Theses and Dissertations

6-30-2016

Temperature Dependent Transport Properties of Chemical Vapor Deposition Graphene with Metal and Metal Hydride Surface Functionalization

Bochen Zhong
University of South Carolina

TEMPERATURE DEPENDENT TRANSPORT PROPERTIES OF CHEMICAL VAPOR
DEPOSITION GRAPHENE WITH METAL AND METAL HYDRIDE SURFACE
FUNCTIONALIZATION

by

Bochen Zhong

Bachelor of Science
Fudan Universtiy, 2007

_____

Submitted in Partial Fulfillment of the Requirements

For the Degree of Doctor of Philosophy in

Physics

College of Arts and Sciences

University of South Carolina

2016

Accepted by:

Richard Webb, Major Professor

Thomas Crawford, Committee Member

Yaroslaw Bazaliy, Committee Member

Goutam Koley, Committee Member

Lacy Ford, Senior Vice Provost and Dean of Graduate Studies

www.manaraa.com

ACKNOWLEDGEMENTS

First of all, I would like to thank my advisor Prof. Richard Webb. He has taught me not only how to be a good experimental physicist but also how to keep positive and optimistic attitude to the life. I appreciate all his contributions of time, ideas, instructions and funding to make my Ph.D. pursuit successful and I learn a lot from him. During these years, he has had a lot of surgeries due to his medical concerns. But whenever he is back to the laboratory from the hospitals, he is always joyful and enthusiastic for scientific research and encourages me to design my own project.

I want to thank Prof. Thomas Crawford and Prof. Yaroslaw Bazaliy for serving my Ph. D. committee and all helpful suggestions and discussion about my dissertation. I would like to express my gratitude to Prof. Goutam Koley from Department of Electrical and Computer Engineering at Clemson University. He provided me not only the good quality home-made CVD graphene samples but also insightful new ideas about this project. I am very grateful to Prof. Koley for his time spent on the driving between Columbia and Clemson to attend the proposal defense and dissertation defense.

I would like to acknowledge my collaborators Dr. Amol Singh and Dr. Ahsan Uddin. Together we worked on this project and solved the problems. I really appreciate all your effort. I thank former and current group members in Dr. Webb's laboratory, including Dr. Samir Garzon, Dr. Yuanzhen Chen, Dr. Longfei Ye, Mr. Ning Lu and Mr. Ken Stephenson. Dr. Samir Garzon and Dr. Yuanzhen Chen trained me with all kinds of

facilities related to sample fabrications and helped me carry out the MTJ noise project which is not included in this dissertation.

Finally, I would give my special thanks to my family members. My parents always provide endless support and passionate love for my whole life. I want to thank my uncle, Mr. Jinfu Zhong, who is the first person to encourage me to pursue higher education in the United State. The Ph.D. life in the United State broadens my sight, enriches my experience and teaches me how to live independently in a foreign country.

ABSTRACT

Graphene, a two-dimensional semi-conductor material containing carbon atoms tightly bonded together in a hexagonal structure, was first isolated by mechanical exfoliation in 2004. Over the past decade, it has drawn huge research interest due to its outstanding mechanical, thermal, and electrical properties. These unique properties of graphene lead to very high carrier mobility. In particular, after an annealing treatment to remove the residual impurities, the suspended graphene mobility exceeds 200,000 cm^2/Vs. However, this value is highly reduced to only a few thousand cm^2/Vs in supported graphene on SiO_2 or SiC substrates, due to different sources of scattering. For example, thermally excited substrate surface polar phonon scattering is the major scattering mechanism in monolayer graphene, while Coulomb scattering becomes the most important scattering mechanism in bilayer or trilayer graphene.

There have been many synthesis methods developed to manufacture few-to-single layer of graphene, such as mechanical exfoliation, epitaxial growth on SiC, chemical vapor deposition (CVD) on Cu or Ni, etc. In our laboratory, graphene is synthesized by CVD method on Cu foils. With CVD grown graphene, temperature dependent carrier mobility and carrier concentration are carried out by the Hall-effect measurement performed in Physical Property Measurement System (PPMS) from temperature range of 300 to 10 K at three different situations: pristine graphene, 2 nm Pd deposited graphene, and Pd decorated graphene with H_2 exposure. For 34 of 35 pristine graphene samples, the

Hall mobility increases when temperature increases, indicating that the mobility is dominated by Coulomb scattering and those samples are bilayer graphene samples. Only one sample behaves as monolayer graphene and shows quantum Hall effect. After 2 nm Pd functionalization layer deposition on those bilayer graphene samples, the mobility decreases due to additional source of scattering induced by Pd functionalization layer. Furthermore, a significant mobility enhancement has been found in the Pd deposited graphene samples with 1000 ppm H_2 exposure. Meanwhile, Coulomb scattering is damped and the dominant scattering mechanism switches to surface optical phonon scattering. All these changes are attributed to the hydrogenation of Pd. The nature of temperature dependent Hall mobility of Pd deposited graphene after H_2 exposure completely matches with the model of semiconductor nanostructures sandwiched by high-κ dielectrics.

TABLE OF CONTENTS

ix

xi

CHAPTER 1

INTRODUCTION

Since its first appearance in 2004 [1], graphene has been extensively studied over the last decade among theorists and experimentalists around the world due to its exceptional mechanical [2], optical [3] and electronic properties [4,5]. Andre Geim and Konstantin Novoselov won the 2010 Noble Prize in Physics for successfully exfoliation of graphene from bulk graphite by Scotch tapes [1].
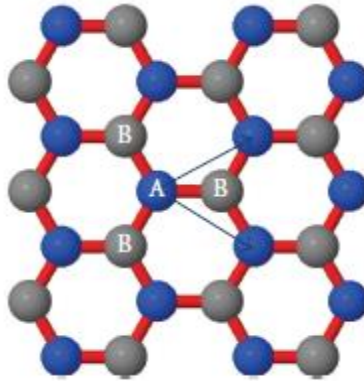
Figure 1.1 Schematic of graphene lattice structure. It can be regarded as two interleaving triangular sublattices A and B [6].

1.1 Electronic Structure of Graphene

Graphene is a two-dimensional (2D) monolayer of carbon atoms bound in a hexagonal lattice, as shown in Fig. 1.1. Each carbon atom is about $a = 1.42$ Å from its

three neighbors in the same plane and shares a sp^2 hybridized σ bond with them. The fourth

bond is a π-bond in the z direction, which is perpendicular to the graphene plane.

These π-bonds from each atom hybridize together to form the π-bands and π*-

bands. These bands are very important because they are responsible for most of the peculiar

electronic properties of graphene [6].
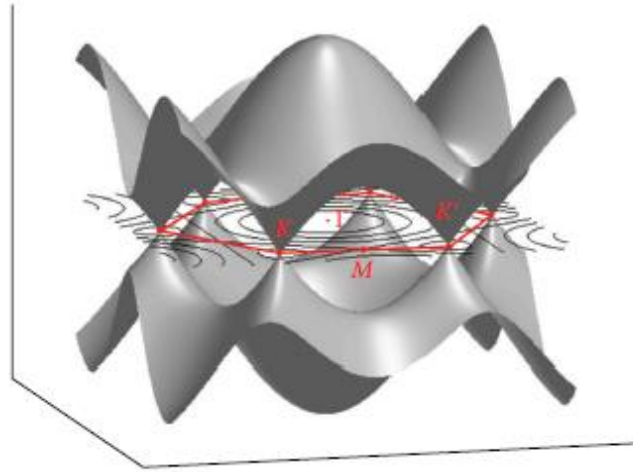
Figure 1.2 First Brillouin zone and band structure of graphene. The vertical axis is energy, and the horizontal plane is the momentum space. *K* and *K'* are the Dirac points. *M* is the midpoint between *K* and *K'*. Γ is the zero point [6].

The hexagonal lattice of graphene can be considered as two interpenetrating

triangular sublattices (see Fig. 1.1). P.R. Wallace mentioned this perspective in 1947 and

used a tight-binding approximation to calculate the band structure of a single graphite layer

which is known as graphene today [7]. From Wallace's work, the tight-binding

Hamiltonian, expressed in a basis of sublattice positions A and B, is given by

$$H = \begin{pmatrix} \varepsilon_A & te^{i\mathbf{k}\cdot\mathbf{a_1}} + te^{i\mathbf{k}\cdot\mathbf{a_2}} + te^{i\mathbf{k}\cdot\mathbf{a_3}} \\ c.c. & \varepsilon_B \end{pmatrix}, \qquad (1.1)$$

2

where $\varepsilon_A = \varepsilon_B = 0$ are the on-site energies of the carbon atoms on sites of A and B, $t \approx 2.7$eV is the nearest neighbor hopping element between A and B sites, $\mathbf{a_1} = a(1,0)$, $\mathbf{a_2} = a(-1/2, \sin[\pi/3])$, $\mathbf{a_3} = a(-1/2, -\sin[\pi/3])$ are the positions of three nearest neighbors, and c.c. is the complex conjugate of the off-diagonal matrix element. The energy bands derived this Hamiltonian are illustrated in Fig. 2 as a function of $\mathbf{k} = (k_x, k_y)$.

From Fig. 1.2, we can find that graphene's conduction and valence bands meets at the Dirac points K and K', which means that graphene has a valley degeneracy of $g_v = 2$. The Dirac points are the major points of interest when one studies the electronic properties of graphene. One of most important electronic properties is the dispersion relation. The dispersion relation of electrons within about ± 1 eV of the Dirac energy is linear, which is expressed as

$$E(\mathbf{k}) = \pm \hbar v_F |\mathbf{k} - \mathbf{K}|, \qquad (1.2)$$

where v_F is the Fermi velocity about

$$v_F = 3at/\hbar \approx 0.9 \times 10^6 \, m/s, \qquad (1.3)$$

or 1/300th speed of light in the vacuum. This linear dispersion relation at low energy allows the charger carrier in graphene act like relativistic particles with an effective speed of light given by the Fermi velocity so that the effective mass of the charge carriers is zero.

Using the linear dispersion relation, the density of states (DOS) close to the Dirac point is derived as Equation 1.4 [8],

$$\rho(E) = \frac{2A_c}{\pi} \frac{|E|}{v_F^2}, \qquad (1.4)$$

where A_c is the unit cell area given by $A_c = 3\sqrt{3}a^2/2$.

The feature of zero band gap makes graphene so special if it is compared to the traditional 2D semiconductors which have finite band gap. The Fermi energy for neutral graphene is at the Dirac point, but it is changeable by impurities or external electric field. However, the Fermi energy in graphene is always within the conduction or valence band while the Fermi energy in traditional semiconductors often falls in the band gap when doping with impurities. In addition, graphene is much thinner than traditional 2D electron gas (2DEG) which is around 5-50 nm. The thickness of graphene is thought to be 3 Å (twice the carbon-carbon bond length).

Transport properties of graphene are also outstanding due to its unique zero band gap structure. For example, it has been reported that the charge carrier density of graphene is tunable by applying electric field at an insulated gate [52,54]. In general, graphene has very high mobility [41,44,55], which makes graphene very suitable for a wide range of applications. We will discuss more details about it in Chapter 3.
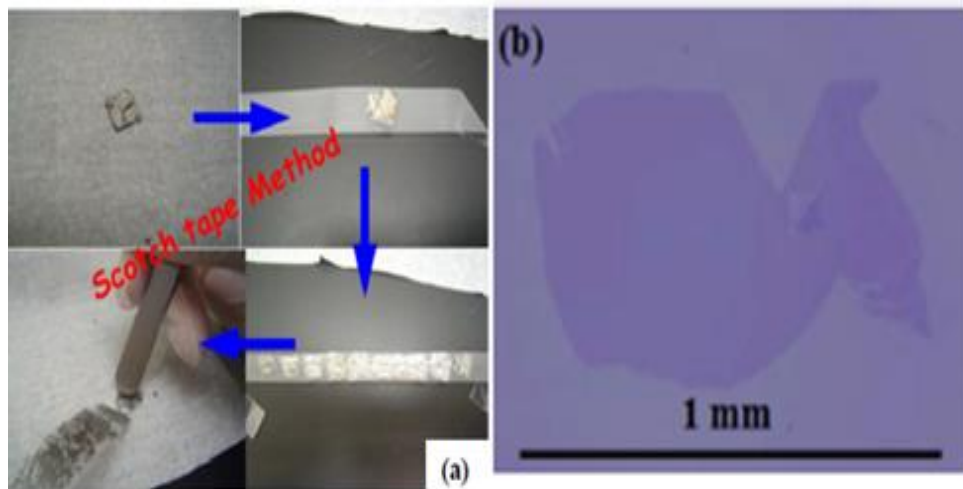
Figure 1.3 (a) Step by step of scotch-tape technique. (b) Large graphene crystal prepared on an oxidized Si wafer by the scotch tape technique (courtesy of Graphene Industries Ltd).

4

1.2 Graphene Synthesis Methods

There have been many graphene synthesis techniques developed to produce few-to-single layer graphene since its first isolation in 2004 by Geim and Novoselov. Every technique has got its own advantages and disadvantages in terms of cost, reliability and quality. In this section, we briefly discuss three different synthesis techniques which are commonly used nowadays and the qualities of the resulting graphene materials.

1.2.1 Mechanical Exfoliation

As mentioned before, the first graphene sample was mechanical exfoliated from highly oriented pyrolytic graphite (HOPG) by the famous Scotch tape. The HOPG was oxygen plasma etched to create 5 μm mesas. Then these mesas were pressed into a layer of photoresist. The photoresist was baked and Scotch tape was used to repeatedly peel flakes of graphite from the mesas. The peeled-off flakes were then released in acetone and captured on the surface of a SiO_2/Si substrate [1]. Using this technique, Geim and Novoselov were able to generate few- and single-layer graphene flakes with dimensions of up to 10 μm. The few-layer graphene flakes were found to have ballistic transport at room temperature and mobility as high as 15000 $cm^2V^{-1}s^{-1}$ on Si/SiO_2 wafers [41]. Five years later, the size of mechanical exfoliated graphene was improved to 1 mm in length [9], of excellent quality and well suited for fundamental research, as shown in Fig. 1.3(b).

Mechanical exfoliation produces excellent quality and high mobility graphene that is well suited for fundamental research. However, this Scotch tape method is a time consuming process and limited to small scale production, which cannot be scaled for industrial production.
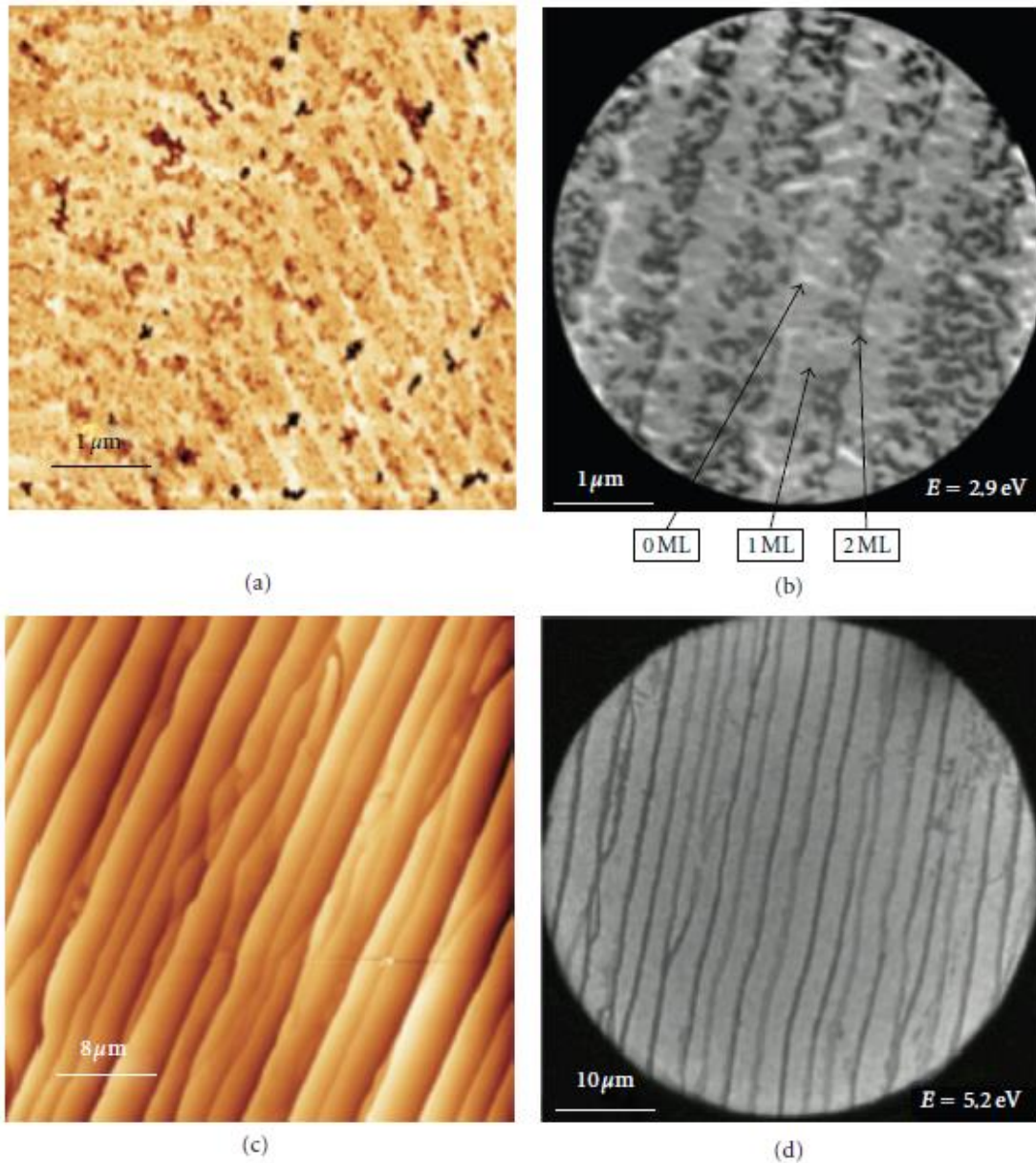
Figure 1.4 Thermal decomposition of SiC grown graphene. (a) AFM image of graphene growth on SiC annealed at UHV. (b) Low-energy electron microscopy (LEEM) image of UHV grown graphene film. (c) AFM image of graphene annealed in Ar at 900 mbar. (d) LEEM image of graphene on Ar annealed SiC substrate [42].

1.2.2 Thermal Decomposition of SiC

The thermal decomposition of silicon carbide is also known as the epitaxial graphene growth. This technique is to heat 6-H or 4-H polytype of SiC to temperatures

6

between 1000 – 1600 °C in ultra-high vacuum (UHV) of 1×10^{-10} Torr. At this temperature, Si sublimates from the surface of SiC and leave behind a carbon-rich surface which rearranges on the hexagonal lattice of SiC to generate single to few-layer graphene depending on the decomposition temperature [10,11]. Using this method, devices were produced with mobility of 1100 $cm^2V^{-1}s^{-1}$ [10]. In 2009, Emtsev *et al.* reported that by heating SiC in Ar at 900 mbar instead of UHV they were able to reduce surface roughness and synthesize much larger continuous graphene layers, up to 50 μm in length, as shown in Fig. 1.4. Mobility was measured up to 2000 $cm^2V^{-1}s^{-1}$ [42]. Juang *et al.* produced millimeter size few- to single-layer graphene sheets using SiC substrate coated in a Ni film. 200 nm of Ni was initially evaporated onto the surface of the SiC and the sample was heated to 750 °C in vacuum later. A continuous graphene layer on the surface of Ni was found [43].

The epitaxial graphene is quite uniform and with large scale which is dependent on the size of SiC wafer. On the other hand, one of the disadvantages of this method is that it is very hard to transfer the graphene to another desired substrate due to the challenges involved in controllably etching SiC. Another disadvantage is the high cost since SiC substrates are very expensive.

1.2.3 Chemical Vapor Deposition

A graphene film can be grown by the chemical vapor deposition (CVD) method on transition metal substrates (e.g., nickel, copper). Li *et al.* annealed the copper foil in a flow of 2 sccm (standard cubic centimeters per minute) hydrogen at a temperature of 1000 °C. Then the copper foil was exposed to methane (CH_4) flow of 35 sccm and pressure of 500 mTorr [12]. Mobility was measured up to 4000 $cm^2V^{-1}s^{-1}$. One year later, Li *et al.* figured

7

out the temperature, methane flow, and methane pressure dependence on the size of graphene domains synthesized by CVD method. It turned out that growth at 1035 $^{\circ}$C with methane flow of 7 sccm and pressure 160 mTorr led to the best quality of grapahene. They were able to improve samples with carrier mobility of up to 16000 cm^{2}V^{-1}s^{-1} [44].
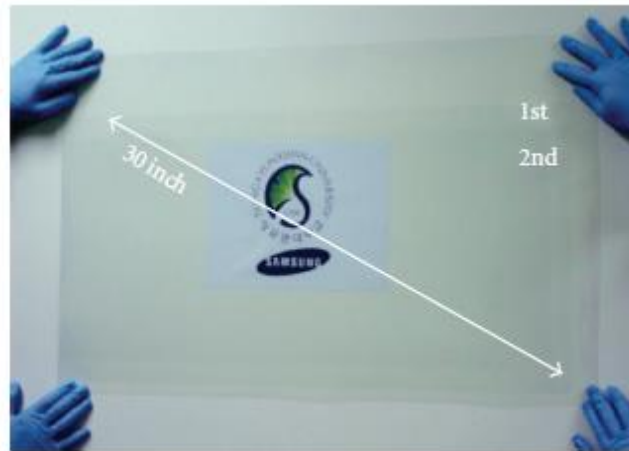
Figure 1.5 Multiple CVD graphene sheets with a diagonal of 30 inches are transferred to PET [13].

In 2010, a roll-to-roll process was reported to produce very large scale graphene layers with a diagonal of 30 inches [13]. Graphene was grown by CVD on copper, and a polymer support layer was adhered to the graphene-copper. The copper was then removed by chemical etching and the graphene film transferred to a polyethylene terephthalate (PET) substrate, as shown in Fig. 1.5. These graphene sheets are superior to commercially available indium tin oxide (ITO) currently used in flat panel displays and touch screens in term of sheet resistance and optical transmittance. In the same year, Lee *et al.* have showed a technique to produce uniform bilayer graphene by CVD on copper using a similar process but with modified growth conditions to be 15 minutes at 1000 $^{\circ}$C with methane flow of 70 sccm and pressure of 500 mTorr. The bilayer nature of the graphene was characterized by Raman spectroscopy, AFM and transmission electron microscopy (TEM) [45]. Fig. 1.6 is

8

showing the 2×2 inch bilayer graphene film on SiO$_2$/Si wafer and Raman spectra of 1 and 2 layers exfoliated graphene and bilayer CVD grown graphene.
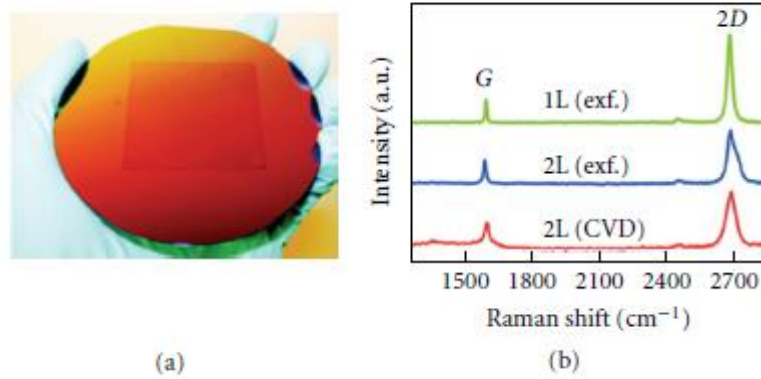
Figure 1.6 (a) 2×2 inch CVD grown bilayer graphene on SiO$_2$/Si wafer. (b) Raman spectra of 1 and 2 layers graphene fabricated by exfoliation and CVD [45].

CVD technique allows the production of large area graphene film which is very important for integrated electronic device and sensors fabrication. An additional advantage is that graphene films can be easily transferred to suitable substrates by etching the metal substrates off. However, the properties of CVD grown graphene deviate to some extent from that of the pristine single-layer graphene (e.g., decrease in mobility and shift in the Dirac point) due to existence of defects and impurities. And the graphene transfer process from the metal substrate to other substrate usually introduces additional impurities and contaminations [14].

1.3 Graphene Applications and Graphene-based Gas Sensors

Nowadays, the semiconductor industry faces a major problem that device scaling is becoming more and more difficult and costly as it is reaching its scientific and technological limits. An alternative path for future development is much needed. People are looking for new materials to replace silicon. Graphene, with the unique properties of

9

zero band gap and linear dispersion relation, is thought to be a potential material for next generation electronic applications.

Figure 1.7 Overview of graphene applications in various areas [15].

1.3.1 Graphene Applications

The atomically thin nature of graphene means that injected charge carriers are confined to a surface just one atom thick. In general, 2D nature of graphene may allow graphene-based devices surpass the obstacles faced by silicon and other conventional semiconductor based electronic and break the limit of device scaling. The various outstanding properties of the graphene enable its applications in diverse areas such as displays and touch screen, terahertz devices, high speed transistors, batteries, supercapacitors, solar cells, high frequency electronics, LED lighting, conductive inks and chemical sensors etc. Fig. 1.7 illustrates possible applications of graphene. Graphene is important not only for its own properties, but also because it is the paradigm for a new

10

class of materials, which follows the rise of graphene technology. For example, hexagonal boron nitride (h-BN) [46,47] and molybdenite (MoS_2) monolayer [48,49] have been reported after the thriving of graphene science and technology. Those 2D nature hexagonal materials are named "beyond graphene". The multiple ways to synthesize such 2D crystals, i.e. by stacking different atomic planes (heterostructures), or by varying the stacking order of homogeneous atomic planes provides a rich toolset for new, customized materials. We expect that the lessons learnt in developing graphene science and technology will drive the manufacturing of many other innovative materials [15].
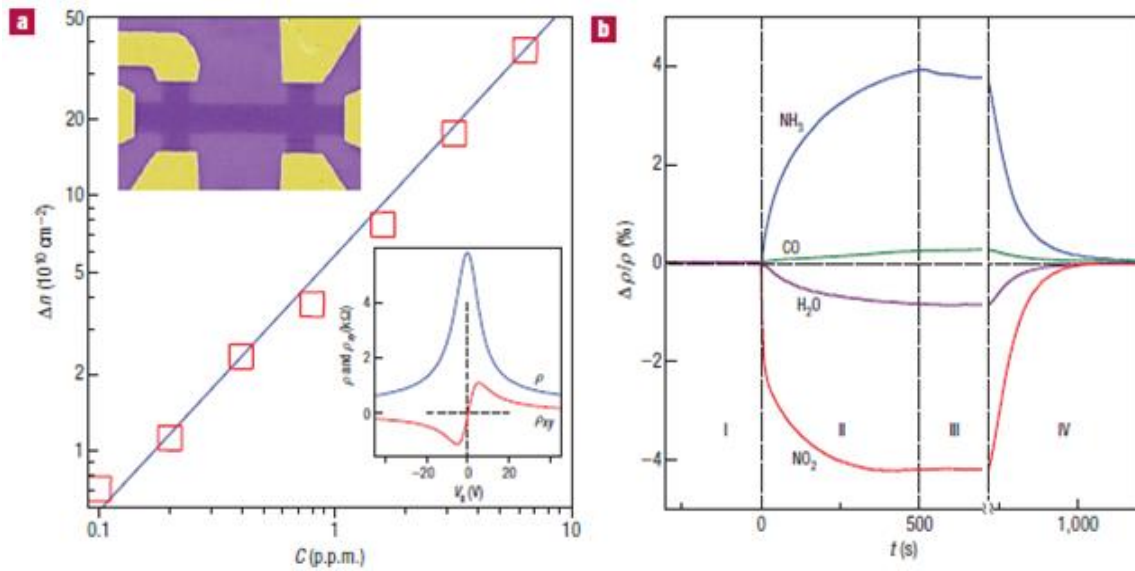
Figure 1.8 Electrical response of graphene to various gases. (a) Concentration Δn of chemically induced charge carriers in single-layer graphene exposed to different concentrations C of NO2. Upper inset: SEM micrograph of this device; the width of the Hall bar is 1 μm. Lower inset: the changes in resistivity ρ and Hall resistivity ρ_{xy} of the device with gate voltage Vg. (b) Changes in resistivity at zero magnetic field as caused by graphene's exposure to various gases diluted in concentration to 1 ppm. Region I: the device is in vacuum; II: analyte exposure; III: evacuation of the experimental set-up; and IV: annealing at 150 °C. For clarity, this transient region between III and IV is omitted.

1.3.2 Graphene-based Gas Sensors

Among these various applications, we are very interested in gas sensing application.

11

The 2D nature of graphene allows analyte molecules to adsorb very efficiently and produce the maximum change in its physical properties. The presence of delocalized π electrons makes it sensitive to a large variety of analytes that can transfer charge to it and change its surface properties. Graphene has high carrier mobility, which will lower the power consumption. In addition, the noise characteristics of graphene have been reported very impressive in the range of 10^{-9} to 10^{-7} Hz^{-1} which is superior to carbon nanotubes [16]. All of these exceptional properties of graphene make it highly suitable for sensing application.

Graphene-based gas sensors are capable of detecting down to a single analyte molecule and integrating large arrays of such sensors would further increase the functional area and improve the sensitivity [17,18]. People have demonstrated various gas sensors based on graphene [17-25]. In 2007, Schedin et al. reported that single molecule detection was achieved with an electrical sensor made of few-layered graphene [17]. Fig. 1.8 shows the electrical response of graphene to various gases. NO_2 and H_2O acting as electron acceptors would decrease the density of electrons in graphene and decrease the resistivity. On the other hand, NH_3 and CO acting as electron donors would increase the density of electrons and increase the resistance of the device.

Although graphene-based gas sensor is sensitive to an extensive variety of polar molecules such as NO_2 and NH_3, it has been reported that pristine graphene is insensitive to H_2 [26]. Therefore, surface functionalization method has been widely utilized to obtain high sensitivity graphene-based H_2 gas sensors [27-30]. By depositing a thin layer of catalytically active noble metals (such as Pd and Pt) on the surface of graphene, charges can transfer between graphene and the metal hydride formed in the presence of H_2, facilitating its detection.

12

Metal nanoparticle (NP) functionalization of 2D materials and its effect on device characteristics and sensing application has attracted significant attention recently. Although people have realized that this method can change the doping of 2D materials [31], enhance sensitivity of sensors by higher adsorption [32] and increase photosensitivity due to electromagnetic scattering [33], there has not been any comprehensive study of the effect of NP decoration and subsequent sensing on fundamental electrical properties such as carrier mobility, carrier concentration, scattering mechanism, etc. This sort of study is very essential to improve the sensor performance and would pave the path for enabling more efficient sensors as well as leading to new applications based on conventional and non-conventional semiconductor materials and devices.

1.4 Outline of the Dissertation

In this dissertation, temperature dependence of carrier mobility and density of CVD grown graphene before and after Pd NP deposition has been investigated by Hall-effect measurement. In the most of pristine graphene samples, the Hall mobility increases as temperature increases, indicating that Coulomb scattering is the most important scattering mechanism. The mobility decreases after 2 nm Pd deposition. Furthermore, mobility of the Pd NP decorated graphene enhances significantly after exposure to H_2 and the dominant scattering mechanism switches to surface optical phonon scattering. This effect can be explained by the high-κ dielectric property of palladium hydride (PdH_x), which strongly damps Coulomb scattering.

Chapter 2 discusses the CVD graphene growth procedures including copper substrate preparation, annealing and final growth phase, etc. Raman spectroscopy characterization which is used to determine the quality of graphene is described next.

13

Fabrication process for hall bar samples, including details of graphene transfer on arbitrary substrate utilizing PMMA assisted transfer technique, photoresist lithography, metal contact pad deposition, and oxygen plasma etching, has been developed for CVD grown graphene.

In Chapter 3, fundamental details of Hall effect are described first. Then, we are going to discuss about the transport properties and scattering mechanisms in monolayer graphene and multilayer graphene.

By the Hall effect measurement from room temperature to 10 K, temperature dependent carrier mobility and carrier density of 35 pristine graphene samples have been carried out in Chapter 4. 34 out of 35 samples show normal Hall effect, while one specific sample exhibits quantum Hall effect (QHE) when it was cooled down to 60 K. This sample is labeled as the QHE device for convenience.

After 2 nm Pd NP deposition on the surface of graphene, temperature dependent carrier mobility and carrier density have been reinvestigated in the first part of Chapter 5. Mobility reduced after 2 nm Pd NP deposition. However, after the exposure to H_2, the Hall mobility significantly enhances and Coulomb Scattering is damped so that the dominant scattering mechanism switches to surface optical phonon scattering. This observation can be explained by the model of semiconductor nanostructures sandwiched by high-κ dielectrics.

At last, Chapter 6 summarizes the dissertation. Possible future work is also briefly discussed.

14

CHAPTER 2

GRAPHENE GROWTH AND SAMPLE FABRICATION

This chapter starts with the CVD graphene synthesis steps including copper substrate preparation, annealing and final growth phase, etc for large area and high quality graphene. Structural and material characterization of as grown and transferred graphene has been carried out by Raman spectroscopy, scanning electron microscopy (SEM) and atomic force microscopy (AFM). Then, fabrication process for hall bar geometry samples is described, including details of graphene transfer on arbitrary substrate using PMMA assisted transfer technique, photoresist lithography, metal contact pad deposition, and oxygen plasma etching.

2.1 Chemical Vapor Deposition: Synthesis of Graphene

Chemical vapor deposistion (CVD) is the technique to grow graphene film on the transition metal substrates (e.g., nickel, copper) by cracking methane (CH_4) in Argon (Ar) and Hydrogen (H_2) ambient at a pressure of ~mTorr and a temperature of ~1000 ºC. There are two possible types of reactions for the CVD process namely homogeneous gas-phase reactions, which occur in the gas phase and may results in formation of powders, and heterogeneous chemical reactions which occur on or near a heated surface leading to the formation of powders or films. In the case of graphene synthesis, homogeneous chemical reactions should be avoided and heterogeneous chemical reactions should be

15

favored during the growth process. The CVD method has demonstrated its ability to grow large area, monolayer, and low defect graphene on inexpensive substrates [12,13].

Figure 2.1 The home-built CVD graphene synthesis system

Fig 2.1 shows the set-up of our home-built CVD graphene growth system. The system consists of the three gas cylinders (CH_4, H_2 and Ar) connected to the corresponding mass flow controllers (MFC) through control valve and stainless steel tubes. The MFCs are MKS Type 1179A. Ar MFC is in 1000 sccm range for flow larger amount of Ar, while H_2 and CH_4 MFCs are respectively in the range of 200 and 50 sccm for keeping CH_4 to H_2 ratio low during the growth. The outputs from MFCs are joined together using a Swagelok Union Cross. One end of the cross is connected to the ¼" quartz delivery tube by a stainless steel bellows. The reaction chamber has a 1½" diameter wide and 2' long quartz tube. The quartz tube is fitted with ¼" thick compressed BN heat blocker at both the ends. The enclosure is formed by stainless steel end caps with sleeves. The sample or substrate is mounted on a flat quartz boat through the outlet on the other end of the chamber. A barometer and a Pirani gauge (MKS 901P, loadlock transducer) are attached to monitor the

pressure of the system. This tubing then connects to the inlet of a mechanical pump (rotary vane pump from Pfeiffer Vacuum of Model: Duo 10 M) which is able to pump down to 4.5 mTorr. However, the base system pressure remains in the range of 100 mTorr. The quartz tube reactor is housed inside a horizontal single zone split tube furnace from Carbolite which is capable of operating at 1100 °C for prolonged hours and takes about 45 min to reach that temperature.
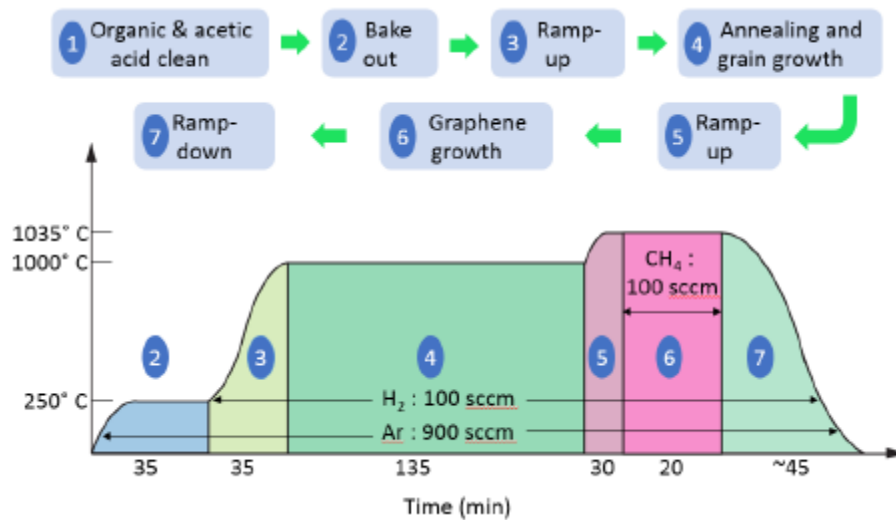
Figure 2.2 Sequence of steps involved in CVD graphene growth on Cu foils. The optimized parameters of the process are shown in the schematic plot.

In our CVD growth system, Cu foils (Alfa Aesar, 99.999% purity) have been chosen as the transition metal substrates over Ni due to the low solubility of C atoms (< 0.001 atoms % at 1000 ℃) in Cu [12]. The Cu substrate preparation requires a good cleaning procedure to get rid of copper oxides such as CuO and Cu_2O in Cu foils. First, the Cu foils are first rinsed and cleaned in acetone and isopropanol (IPA), and then sonicated in acetic acid to remove oxide. After loading the Cu foil under Ar over pressure, the growth chamber is evacuated and then Ar is flown at 250 ℃ for bake out. Subsequently, H_2 is flown for 2 hours at 1000 ℃ to anneal Cu to increase its crystalline quality and remove any remaining

17

and newly formed oxide. Next, the actual growth is performed at temperature of 1035℃ in presence of CH_4. The last step is to cool down the furnace and take the samples out.
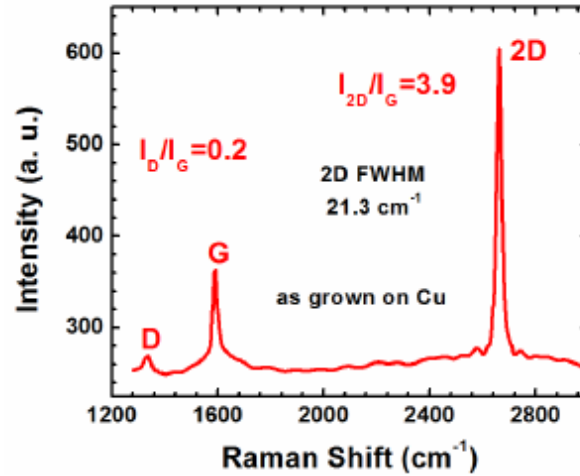
Figure 2.3 Raman spectrum of CVD graphene as grown on Cu foil.

2.2 Structural and Material Characterization of Graphene

To determine the quality of our CVD graphene samples, Raman spectra are scanned to provide quick and immediate feedback on as-grown graphene on Cu foils [34]. Raman spectroscopy is based upon vibrational spectrum of a material system. It is sensitive to strain and can detect stress in the semiconductor in very small region [35]. For our study, Horiba LabRAM 1B Raman Spectrometer has been used.

There are three important peaks in the Raman spectra of graphene: G, D and 2D bands at ~1580, 1350 and ~2700 cm^{-1} respectively [36]. The presence of G peak confirms the presence of carbonaceous material with sp^2 bonding and its intensity is proportional to the thickness of the carbonaceous material. The D band is defect related peak in graphene, which only occurs when the periodicity of hexagonal lattice is broken by a point defect, grain boundary, line defect, graphene edge, dopant atom etc [37]. The other prominent

18

band 2D helps in determining the number of layers in the sample, based on the shape and width of 2D band.

Fig. 2.3 shows the Raman spectrum of as grown graphene samples on Cu. The I_D/I_G ratio is less than 0.2, indicating good quality of the graphene with very low defect density [38]. The I_G/I_{2D} ratio of 3.9 and 2D peak full width at half maximum (FWHM) of ~21.3 cm^{-1} indicate the presence of single layer graphene [34].
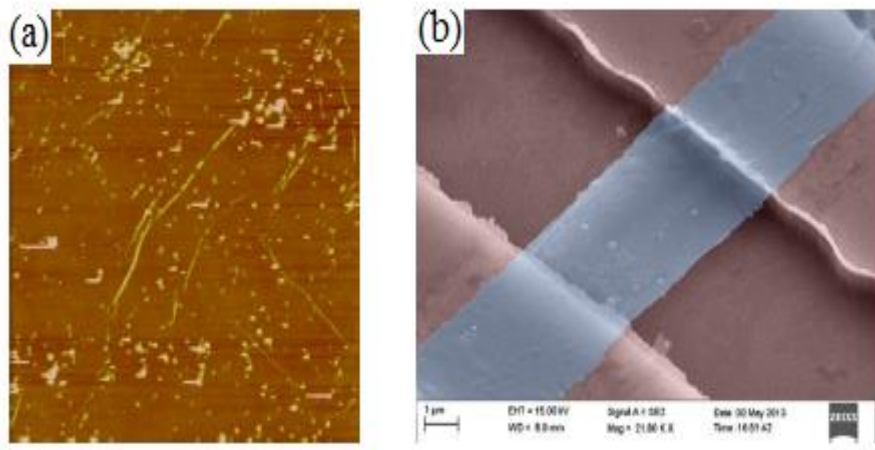
Figure 2.4 (a) 20×20 μm^2 AFM image of transferred graphene on SiO_2/Si substrate without annealing. (b) False color SEM image of suspended graphene over the trench on SiO_2/Si substrate.

AFM image of transferred graphene on SiO_2/Si substrate just after transfer without any annealing is shown in Fig. 2.4(a). This image shows the PMMA residues along with a few wrinkles. It has been reported that annealing at 300-400 ^{o}C after transfer removes significant amount of PMMA residue and graphene becomes much cleaner [39]. Fig. 2.4(b) shows the false color high resolution SEM image of suspended graphene with uniform structural quality and monolayer thickness on the SiO_2/Si substrate. The trench under the graphene is etched off by wet etching method.

19
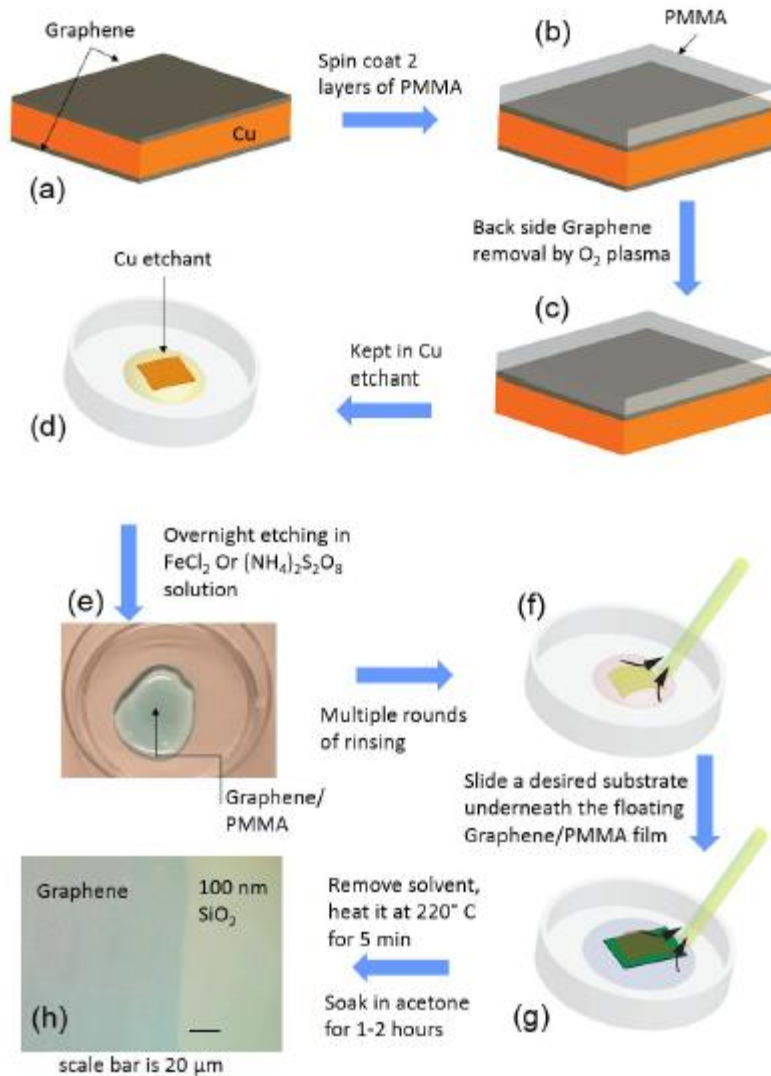
Figure 2.5 Sequence of steps for graphene transfer on any desirable substrate.

2.3 Graphene Transfer

The CVD grown graphene on the transition metal substrate cannot be used directly for device fabrication or sensing applications. It needs to be transferred on a desired substrate which is suitable for the characterization and other applications. In the growth furnace, the Cu foils have graphene on both sides and graphene on the bottom side is in general inferior quality as compared to the one grown on the top side. We just use the top

side graphene which has better quality. The top side graphene was protected by spin coating poly methyl methacrylate (PMMA) twice at 2000 rpm for 40 sec resulting in approximately 800 nm thickness. The layer of PMMA also provided mechanical strength to graphene in the subsequent processing steps. The PMMA coated sample was mounted upside down in reactive ion etching (RIE) chamber in order to remove the bottom side graphene layer by O_2 plasma at 150 W RF power and 300 mTorr pressure for 180 sec. The sample was then soaked in concentrated Cu etchant ($FeCl_3$ or $(NH_4)_2S_2O_8$) over night for complete removal of Cu. After that, the floated graphene was rinsed multiple times in deionized water (DI). A desired substrate can then be slid underneath the floating graphene/PMMA and scooped off from the liquid solution. The substrate with transferred graphene/PMMA was allowed to dry in air and then baked at 220 ˚C in order to reduce the wrinkles in graphene originated while transfer on substrate. The sample was then kept in acetone for 2-3 hours to remove PMMA from top of transferred graphene. Organic cleaning of the sample in acetone and IPA was the last step.

2.4 Hall Bar Sample Fabrication

To fabricate the Hall bar graphene samples, we chose the SiO_2/Si substrate. The highly doped Si has low resistivity in the range of 0.008–0.02 Ω-cm and the SiO_2 with thickness of 300 nm acts as the insulator. Firstly, the SiO_2/Si substrate was lithographically patterned and 10/80 nm Ti/Au were deposited by electron beam evaporation method at a base pressure of 10^{-6} Torr for metal contact. Secondly, the whole film of graphene was transferred onto the substrate as described in section 2.2 but the PMMA supporting layer was not dissolved to prevent contaminations from the following photolithography step.

Next, second level photolithography was done to define the active graphene area for Hall
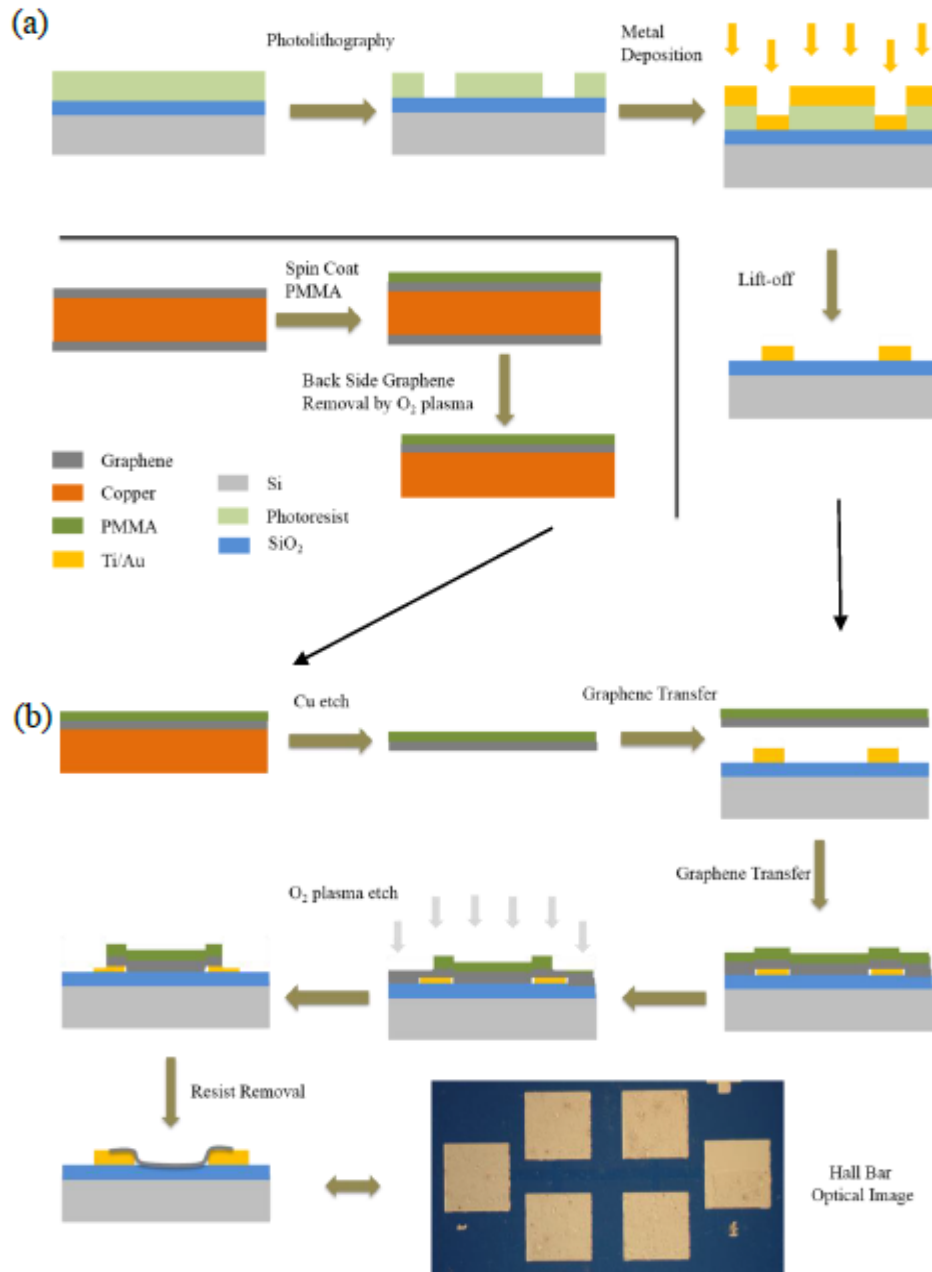
Figure 2.6 Hall bar graphene sample fabrication procedure. (a) Metal contact pads on SiO_2/Si substrate and graphene pre-transfer steps. (b) Graphene transfer, Hall bar channel patterning, O_2 plasma etching and optical image of one fabricated small area sample.

bar geometry. Afterwards, unwanted graphene with PMMA was etched by O_2 plasma in

RIE chamber. Finally photoresist and PMMA were dissolved in Acetone and Methanol.

We fabricated two sizes of Hall bar graphene samples: the size of small sample is about 20 μm × 200 μm, while the size of large sample is approximately 100 μm × 600 μm. Measurement of both small and large area devices were carried out for pristine graphene but Pd NP deposition and subsequent H_2 characterization were only performed in large area devices for two reasons. First, Pd NP deposition requires shadow
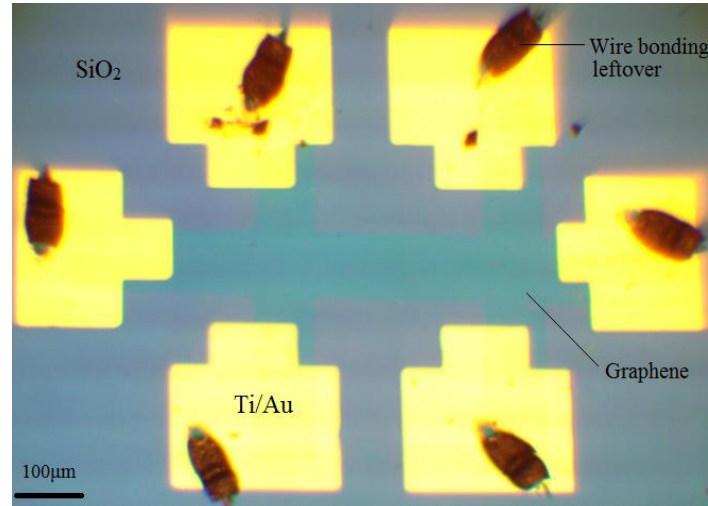
Figure 2.7 Optical image of one large area graphene device with wire bonding marks on the metal pads and graphene channel is pretty clear in the middle.

masks to cover the sample completely except the channel region. It is difficult to align shadow masks very well on the small size devices under our laboratory's conditions. For easy shadow masking, active graphene channel of the Hall bar samples is kept in the range of several hundred micrometers. Second reason is that the small width channel is pretty easy to be damaged or broken during the later processing steps even though the alignment might be good. Complete fabrication process is shown in Fig. 2.6 along with the optical image of graphene Hall pattern (20 μm channel width) in the bottom. Fig. 2.7 is the optical

23

image of one large area device which will be used to do Pd NP deposition after the initial

pristine graphene transport properties characterization.

CHAPTER 3

HALL EFFECT, SCATTERING MECHANISMS AND TRANSPORT PROPERTIES OF GRAPHENE

3.1 Hall Effect

The Hall effect was discovered in 1879 by Edwin Herbert Hall [40]. It describes the movement of free carriers in a conductor or semiconductor when applying an electric current and a magnetic field perpendicular to the current. It is one of the important techniques to measure the transport properties (such as carrier mobility and carrier density) in semiconductors.
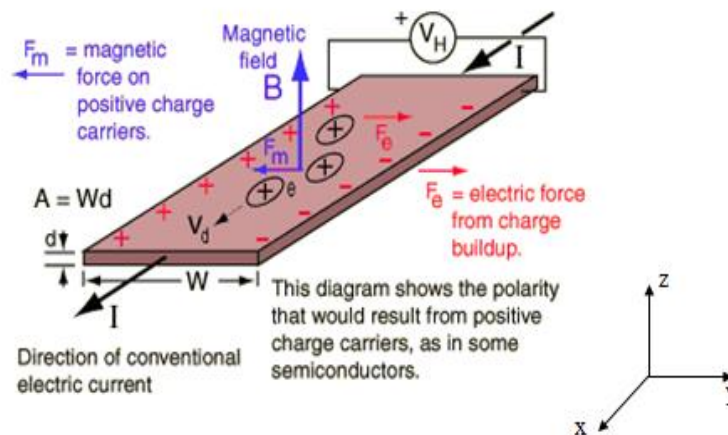
Figure 3.1 Hall effect diagram for p-type doping semiconductors [50].

The experimental setup for Hall measurement is shown in Fig. 3.1. Considering a p-type doping semiconductor with a rectangular cross section area of *A* placed in a

25

magnetic field *B* along the z-direction, a dc current *I* is applied along the x-direction. For the p-type semiconductor, the holes travel along the x-direction with a velocity v_x. The magnetic field causes a Lorentz force on the accelerated charge carriers in a direction dictated by the right hand rule. The resulting force along the negative *y*-direction F_m deflects the holes from its original moving path along the x-direction to the negative y-direction, which leads to the charge accumulation across the sample. However, to reach equilibrium, the force, F_m is balanced by an electric force from charge buildup, F_e, so that there is no net force on the holes and the electric force develops the Hall voltage, V_H across the sample in the negative *y*-direction. The Lorentz force acting on the holes is given by:

$$\vec{F} = q(\vec{E} + \vec{v} \times \vec{B}) . \tag{3.1}$$

Considering initial conditions discussed above, the Lorentz force can be further expressed as:

$$\vec{F} = q\vec{E} + \begin{pmatrix} \vec{e_x} & \vec{e_y} & \vec{e_z} \\ v_x & 0 & 0 \\ 0 & 0 & B_z \end{pmatrix} = qE_x\vec{e_x} + q(E_y - v_xB_z)\vec{e_y} + qE_z\vec{e_z} . \tag{3.2}$$

In the steady state, the y and z component of the force must be zero, which yields to the relation below:

$$F_y = q(E_y - v_xB_z) = 0 . \tag{3.3}$$

Introducing the current density $J_x = qpv_x$, the y-component of electric field can also be rewritten as a function of the current density as

$$R_y = v_xB_z = \frac{J_x}{qp}B_z , \tag{3.4}$$

where q is the holes density. This electric field along y-direction is called the Hall field. The Hall coefficient, R_H, is defined as the Hall field divided by the applied current density and magnetic field:

$$R_H = \frac{E_y}{J_x B_z}.$$ (3.5)

Comparing Eq. (3.4) to Eq. (3.5), we can get

$$R_H = \frac{E_y}{J_x B_z} = \frac{1}{qp}.$$ (3.6)

Since $E_y = V_H / W$ and $J_x = I_x / A = I_x / Wd$, Eq. (3.6) can be rewritten as

$$R_H = \frac{V_H d}{I_x B_z}.$$ (3.7)

From Eq. (3.6) and Eq. (3.7), the carrier density p is given by

$$p = \frac{I_x B_z}{q V_H d}.$$ (3.8)

Furthermore, combining the conductivity $\sigma = qp\mu$, we have the expression of carrier mobility here

$$\mu = \frac{\sigma_{xx} V_H}{IB}.$$ (3.9)

From the sign of the Hall voltage, the type of semiconductor (n-type or p-type) can be determined easily.

3.2 Electric Field Effect in Graphene

Due to its unique band structure, graphene shows novel transport effects such as electric field effect and minimum conductivity which are absent in most conventional materials [51]. Electric field applied perpendicular to graphene plane can induce charge carriers, also referred as electric field effect. The Fermi level (E_F) can move up to

27

conduction band which induces electrons, and can move down to valance band which induces holes depending upon the direction of the external electric field. The gate voltage induces a surface charge density $n = \varepsilon_0 \varepsilon V_g / te$ where $\varepsilon_0 \varepsilon$ is the permittivity of the insulator layer, e is the electron charge, and t is the thickness of the insulator layer [6]. Without externally applied electric field, the E_F should ideally be coinciding with the Dirac point in graphene and n should theoretically vanish [52]. However, in graphene samples there is always finite charge present due to either thermally generated carriers, electrostatic spatial inhomogeneity or carrier induction from impurities at graphene and substrate interface even in absence of applied electric field [53].
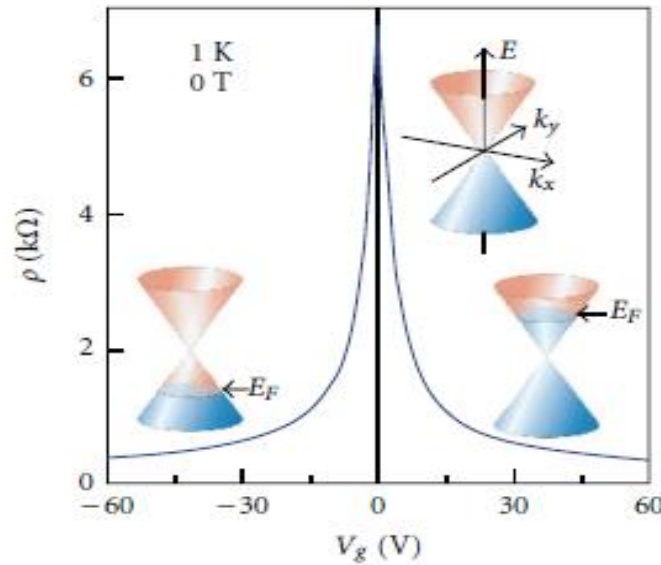
Figure 3.2 Ambipolar effect of a single-layer pristine graphene. The insets show the changes in the position of the Fermi level E_F as a function of gate voltage V_g [52].

On the other hand, the charge carrier density in graphene channel can be easily tuned by applying electric field at an insulated back gate. From Fig. 3.2, E_F is below the Dirac point at negative back gate V_g and for positive V_g, E_F goes above it [52]. Generally,

28

the charge density can be tuned from 10^{11} to 10^{13} cm^{-2} by applying a gate voltage that moves E_F 10 to 400 meV away from the Dirac point [54].

3.3 Conductivity and Scattering Mechanisms in Graphene

In contrast with ideal graphene, experimental graphene has defect [56] and impurities [57,58], forms edges and ripples during the growth process[59], and interacts with phonons [5, 55]. By introducing the spatial inhomogeneities in the carrier density, these perturbations change the electronic properties of an ideal graphene sheet when the Fermi level is close to the Dirac point and alter the minimum conductivity of graphene. Furthermore, they act as scattering sources to reduce the electron mean free path and affect the carrier mobility when the Fermi level is away from the Dirac point [54]. From a theoretical point of view, two different transport regimes are described depending on the mean free path length l and the graphene length L. When $l > L$, transport is called ballistic transport since carriers can travel at Fermi velocity v_f from one electrode to the other without scattering. In this regime, transport follows the Landauer formalism [60], and the conductivity is expressed as

$$\sigma_{ball} = \frac{L}{W} \frac{4e^2}{h} \sum_{n=1}^{\infty} T_n , \qquad (3.10)$$

where W is the width of graphene and the sum is over all available transport modes of transmission probability T_n. This theory predicts that at the Dirac point the minimum conductivity is

$$\sigma_{min} = \frac{4e^2}{\pi h} = 4.92 \times 10^{-5} \Omega^{-1} . \qquad (3.11)$$

On the other hand, when $l < L$, carriers move around with elastic and inelastic collisions and transport goes into the diffusive regime. This regime occurs when the carrier

29

density n is much larger than the impurity density n_i. In this regime, transport is often described by the semi-classical Boltzmann transport theory [61]. At very low temperature, the conductivity can be expressed as

$$\sigma_{sc} = \frac{e^2 v_f \tau}{\hbar} \sqrt{\frac{n}{\pi}} , \qquad (3.12)$$

where τ is the total relaxation time. This equation shows that the diffusion of carrier scattering is independent on the impurity density n_i. The total relaxation time τ plays a big role here and depends on the scattering mechanism which dominates the transport system or a combination of multiple scattering mechanisms if no one dominates. There are several scattering mechanisms mostly discussed in the literature: Coulomb scattering by charged impurities (long-range scattering), short-range scattering (defects, adsorbates), and electron-phonon scattering. We will briefly discuss these scattering mechanism and relevant transport measurements one by one in the following part.

3.3.1 Coulomb Scattering

Coulomb scattering is also known as long-range scattering. It comes from the long-ranged variations in the electrostatic potential caused by charged impurities close to the graphene film. These impurities are thought of as trapped ions in the underlying substrate, but it remains under debate [67]. Assuming the semiclassic model has a random distribution of charged impurity density n_i, it was predicted that the charged impurity scattering is proportional to $\sqrt{n}/n_i$ [62]. Based on Eq. (3.12), the conductivity at high carrier density ($n \gg n_i$) is given by

$$\sigma_i = \frac{Ce^2}{h} \frac{n}{n_i} , \qquad (3.13)$$

30

where C is a dimensionless parameter related to the scattering strength. Considering the dielectric screening from the SiO$_2$ substrate and the random-phase approximation, it was estimated that $C \approx 20$.
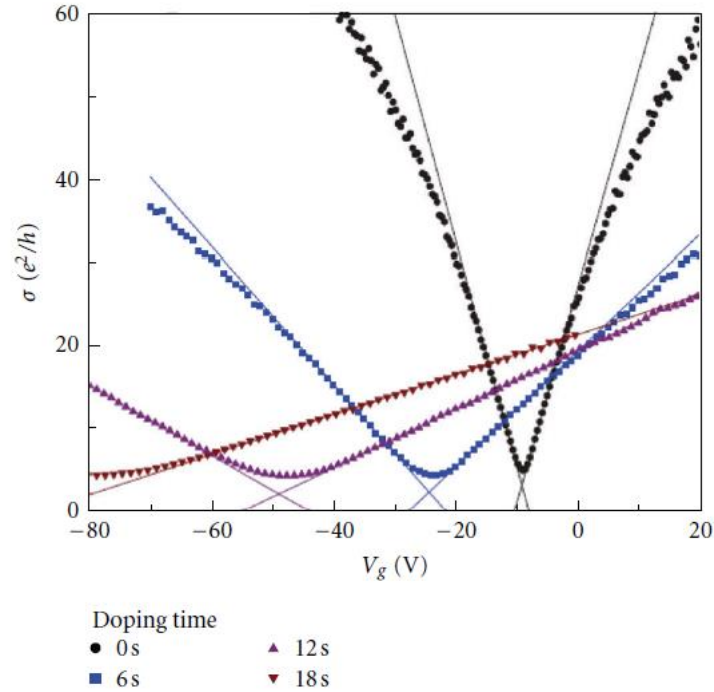
Figure 3.3 Effect of charge impurities on transport properties of graphene. The conductivity versus gate voltage for a pristine sample (black curve) and three different potassium doping concentrations at 20 K in UHV are presented. Lines represent empirical fits [57].

In 2008, Chen et al. experimentally doped a graphene film with a controlled potassium flux in UHV to investigate the effect of charged impurities on the graphene conductivity and carrier mobility [57]. Fig. 3.3 shows the conductivity as a function of gate voltage for a pristine graphene sample and three different potassium doping concentrations. It can be clearly seen that the back gate voltage of the minimum conductivity becomes more negative with increasing the amount of potassium doping. Since potassium atoms dope graphene with electrons, the Fermi level of graphene moves up with respect to the

31

Dirac point [17]. One can also see that $\sigma(V_g)$ looks more linear and mobility decreases as the doping concentration n_i increases which is in good agreement with Eq. (3.13).

3.3.2 Phonon Scattering

Phonons can be considered an intrinsic scattering source since they limit the mobility at finite temperature even when there is no extrinsic scattering source. As discussed in Chapter 1, the dispersion relation of graphene consists of six branches. Longitudinal acoustic (LA) phonons are known to have a higher electron-phonon scattering cross-section than those in the other branches [63]. The LA phonon scattering can be considered quasi-elastic since the phonon energies $\hbar\omega_q$ are negligible in comparison with the Fermi energy of electrons E_F. In order to determine the effect of electron-phonon scattering on transport of graphene, one must consider two distinct transport regimes separated by a characteristic temperature T_{BG} called the *Bloch-Grűneissen* temperature [63], defined as

$$k_B T_{BG} = 2k_F v_{ph},\tag{3.14}$$

where k_B is the Boltzmann constant, v_{ph} is the sound velocity, and k_F is the Fermi wave vector with reference to the K point in the BZ:

$$k_F = \sqrt{n\pi},\tag{3.15}$$

where *n* is the electron density in the conduction band [64]. If the graphene carrier density *n* is in the scale of 10^{-12} cm^{-2}, we have $T_{BG} \approx 54K$. For $T \gg T_{BG}$, the Bose-Einstein distribution function for the phonons is $N(\omega_q) \approx k_B T / \hbar\omega_q$, which gives rise to a linear

32

temperature-dependence of the scattering rate and hence the resistivity $\rho \sim T$. When $T \ll T_{BG}$, $\rho \sim T^4$ was obtained [63], as shown in Fig. 3.4.
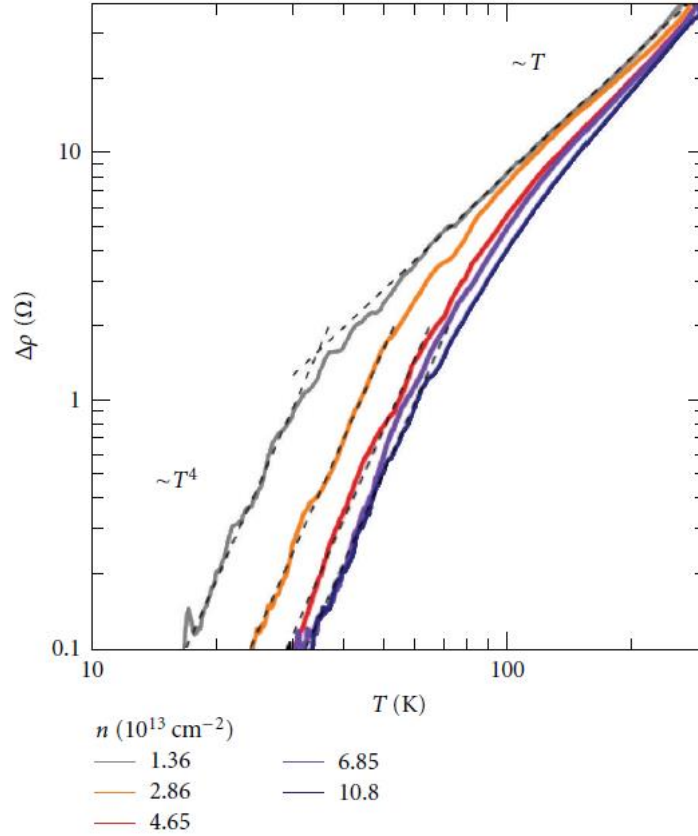
Figure 3.4 Electric resistivity of graphene over wide range of T [65].

3.3.3 Short-range Scattering

Short-range defects such as vacancies and cracks in graphene are predicted to produce midgap states in graphene [66]. We modeled vacancies as a deep circular potential well of radius R and this strong disorder leads to a conductivity which is roughly linear in n:

$$\sigma_d = \frac{2e^2}{\pi h} \frac{n}{n_d} \ln^2(\sqrt{\pi n}R), \qquad (3.16)$$

33

where n_d is the defect density. Eq. (3.16) is similar to Eq. (3.13), the one for charge impurities, with an extra logarithmic term which is dependent on the charge carrier density.
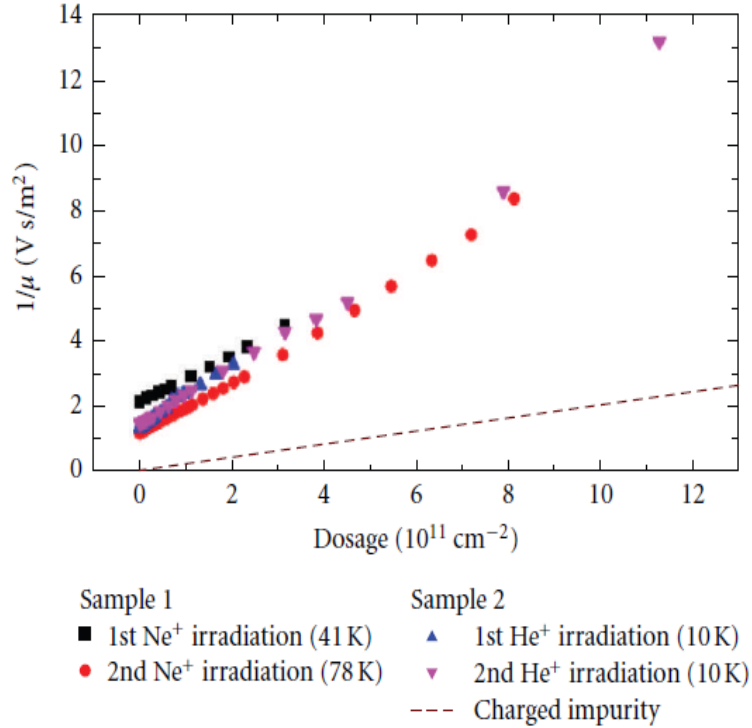
Figure 3.5 Inverse of mobility ($1/\mu$) as a function of ion dosage for different samples and irradiated ions (Ne$^+$ and He$^+$). The dashed line corresponds to the behavior for the same concentration of potassium doping [56].

Defect scattering was experimentally investigated by irradiating a graphene flake with 500eV He and Ne ions in UHV [56]. The resulting conductivity was also demonstrated to be approximately linear with charge density, and with mobility inversely proportional to the defect dose n_d. As shown in Fig. 3.5, the mobility of defect sample was found to be 4 times larger than the same concentration of charged impurities. Comparing the linear fits of Figure 3.5 with Eq. (3.16), the defect potential well radius R was fitted to be $R \approx 2.9\,\text{Å}$ which is reasonable for a single carbon vacancy.
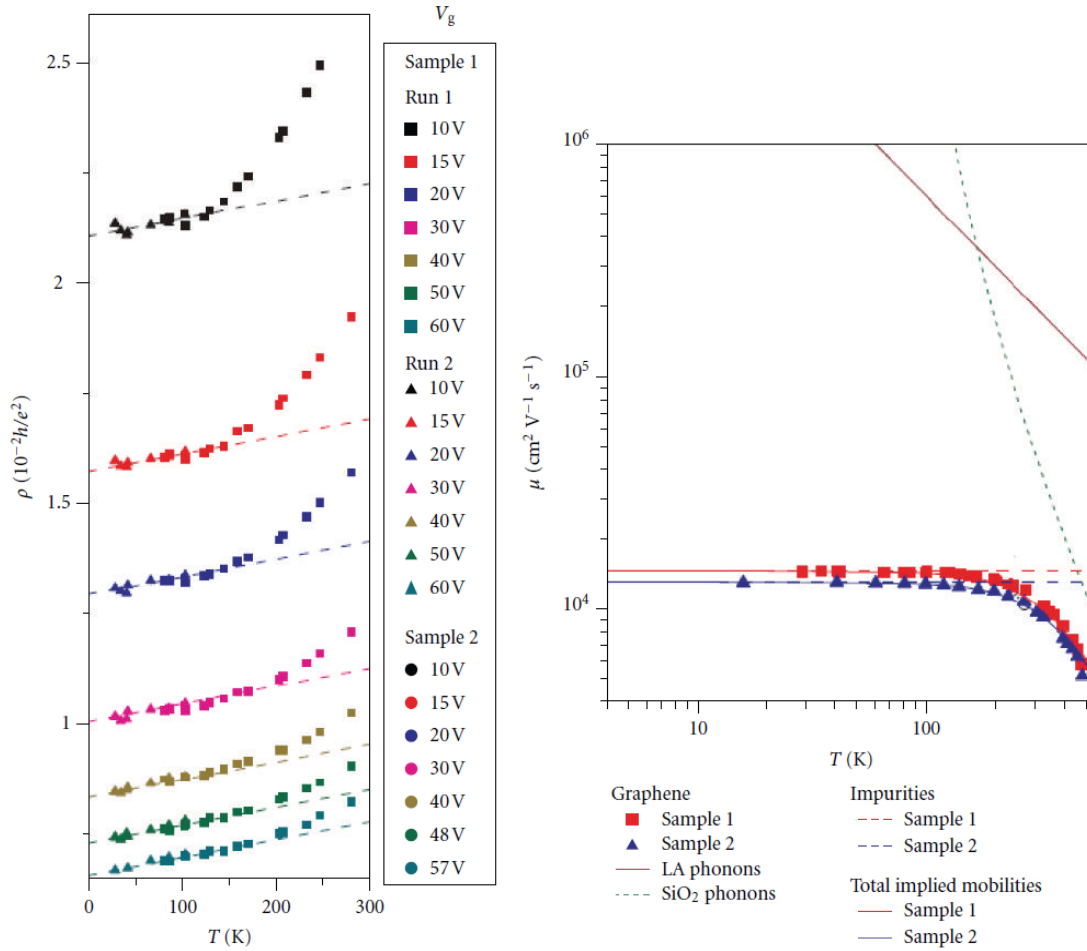
Figure 3.6 (a) Temperature-dependent resistivity of graphene on SiO_2 for different gate voltages, samples, and runs. Dashed lines are linear fits at low temperature. (b) Temperature-dependent mobility in graphene on SiO_2 for two samples at $n = 1 \times 10^{-12} \, cm^{-2}$. Mobility limits due to LA phonons (dark red solid line), substrate surface phonons (green dashed line), and impurities (red and blue dashed lines) for two samples are presented [5].

3.4 Carrier Mobility in Graphene

In a graphene-based electronic device, all of the scattering mechanisms mentioned above should be considered. From a technological point of view, determining the exact nature of the scattering mechanism that limits the mobility is very important to develop high-speed electronic devices. To do so, one must also take into account the effect of the underlying substrate on the electronic transport.

3.4.1 Graphene on SiO₂

The most commonly-used substrate is SiO₂ substrate. Chen et al. did a general study of scattering mechanisms in graphene on SiO₂ by measuring the temperature dependence of the ambipolar effect [5]. The resistivity was fitted using three terms: $\rho(n,T) = \rho_0(n) + \rho_{LA}(T) + \rho_{SPP}(n,T)$. Each term was associated with a certain scattering mechanism. As shown in Fig. 3.6 (a), the first two terms were determined with a linear fit at low T. The y-intercepts represent $\rho_0(n)$ and were found to scale linearly with n^{-1}. Based on Eq. (3.13) and Eq. (3.16), this observation can be attributed to charged impurities and defects. $\rho_{LA}(T)$ was determined by the slope of the linear fit in Figure 3.6(a) and appeared to be independent of the charge density. These results agree well with predictions for longitudinal acoustic (LA) phonon scattering in the regime where $T \gg T_{BG}$ discussed in the section 3.3.2. At last, the third term ρ_{SPP} was found to have strong temperature dependence. Such behavior is explained by the existence of surface polar phonons (SPP) in the SiO₂ substrate which produce an electrical field that couples to carriers in graphene.

Fig. 3.6 (b) shows the temperature-dependent mobility and the theoretical limits of the three scattering mechanisms (LA phonons, SPP, and Coulomb/impurities). At room temperature, SPP and impurities are by far the two dominant scattering mechanisms for graphene on SiO₂. At low temperature, mobility is mainly limited by the SPP scattering. Typically, mobility of graphene on SiO₂ ranges from a few thousands to 15000 cm²V⁻¹s⁻¹.
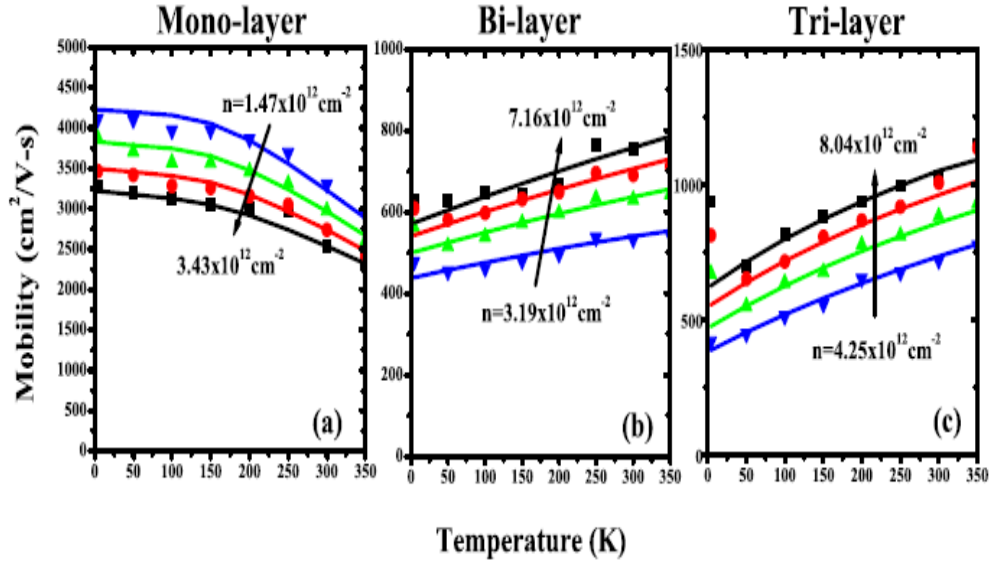
Figure 3.7 Temperature dependent of Hall mobility at various carrier densities in (a) monolayer graphene, (b) bilayer graphene, and (c) trilayer graphene. The symbols are the measured data, the lines are fits [68].

In 2009, Zhu et al. systematically investigated the carrier density and temperature dependence of mobility in exfoliated monolayer, bilayer, and trilayer graphene by measuring Hall effect [68]. As illustrated in Fig. 3.7, for monolayer, the mobility decreases with increasing temperature primarily due to the substrate surface polar phonon scattering [5, 68-70]. The SiO₂ optical phonons at the substrate/graphene interface modulate the polarizability, which generates an electric field that couples to the charged carriers in graphene. The coupling or the field depends exponentially on the substrate graphene distance. At the Van der Waals distance of about 0.35 nm, it is much stronger than the coupling of the carriers to the LA phonons of graphene. Since the substrate surface polar phonon scattering is proportional to the phonon population number, the scattering rate can be expressed as: $\tau_{OX}^{-1} \propto \Sigma_i \dfrac{c_i}{e^{\hbar\omega_i/k_B T} - 1}$, where $\hbar\omega_i$ is the phonon energy. For SiO₂, there are two major surface phonon modes at $\hbar\omega_1 = 59$ meV and $\hbar\omega_2 = 155$ meV with the ratio of

$c_2 / c_1 \approx 6.5$, which is determined by the dielectric constants in SiO$_2$ [69]. Thus, as the temperature is increased, the mobility is expected to decrease drastically.

On the other hand, in bilayer and trilayer graphene, the mobility increases with temperature because the electric field of the substrate surface polar phonons is effectively screened by the additional graphene layer(s) and the mobility is dominated by Coulomb scattering [68,71,72]. Since bilayer graphene has a parabolic band structure, the energy averaging of the Coulomb scattering time leads to the mobility increasing proportionally with temperature: $\mu \propto k_B T$ [73]. The dielectric screening, which we ignored in the above analysis, could also introduce additional temperature dependence.

Effect of short-range scattering and LA phonon scattering do not vary with temperature. Since the density of states, the matrix element and the screening function are energy independent for bilayer graphene, mobility limited by short-range scattering is independent of temperature. In monolayer graphene, when $k_B T << E_F$, the temperature dependence of conductivity and hence mobility that is limited by short range scattering is nearly constant [74]. On the other hand, the mobility limited by LA phonons in monolayer graphene is inversely proportional to temperature [75]. However, since the magnitude of the mobility limited by LA phonon scattering is in the order of 10^5 cm^2/Vs [55,63,76], much larger than the mobilities limited by the Coulomb and surface polar phonon scattering mechanisms discussed here, effect of acoustic phonon can be neglected for bilayer graphene.
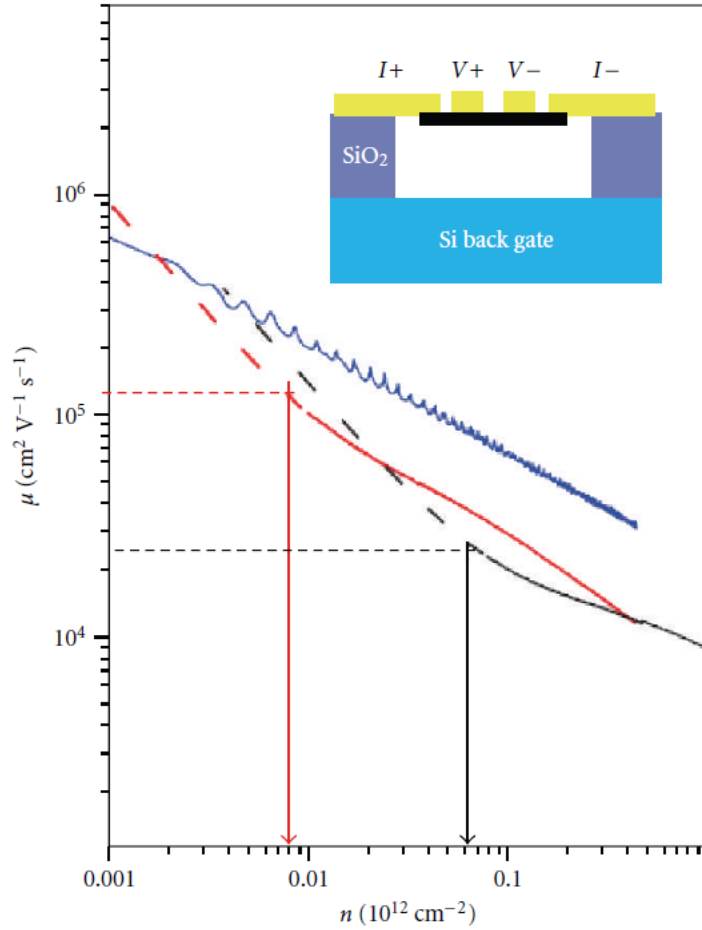
Figure 3.8 Mobility versus charge density for suspended (red line) and nonsuspended (black line) graphene at $T = 100$ K. The blue line represents the ballistic model prediction. Inset: schematic representation of the suspended graphene device [76].

3.4.2 Suspended Graphene

One possible way to improve the carrier mobility is to remove the substrate to make graphene suspended. In 2008, this approach was investigated by two groups, in which the authors fabricated suspended graphene devices by chemically etching the underlying SiO_2. Du et al. [76] obtained the carrier mobility of suspended graphene as

high as 100,000 cm^2/Vs at T = 100 K for charge density below 8×10^{-9} cm^{-2}, as shown in Fig. 3.8.
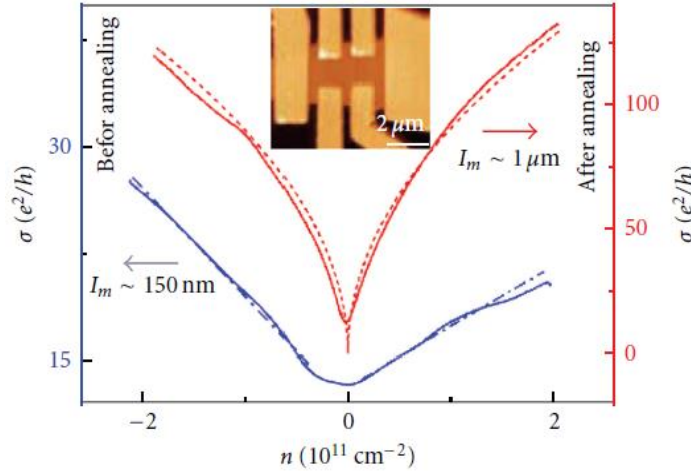
Figure 3.9 Conductance versus gate voltage (at T = 40 K) for a suspended graphene device before (blue line) and after (red line) annealing and current-induced cleaning. The red dotted line was calculated using a ballistic model. Inset: AFM image of the suspended graphene device [55].

Bolotin et al. [55] demonstrated at low temperature, suspended current-annealed graphene can sustain near-ballistic transport over micron dimensions. Fig. 3.9 shows that mobility and mean free path *l* clearly increase after current-induced cleaning and high-temperature annealing of the device. At high temperature, the resistivity of such high-quality graphene increases linearly with T, suggesting that LA phonon scattering dominates in suspended graphene. At low temperature (~5K), mobility as high as 170,000 cm2/Vs was obtained and the mean free path reached the device dimension.

3.4.3 Other Substrates

Although suspended graphene shows impressive transport properties, this geometry puts evident constraints on the device architecture. Another possible way to improve the carrier mobility is to use a substrate which is free of trapped charge. Boron nitride (BN)

40

was proposed as a substrate to satisfy this requirement [77]. Compared to SiO_2, BN has an atomically smooth surface, is relatively free of charged impurities, and has a lattice constant similar to that of graphene and high surface phonon frequencies. All these advantages result in a mobility about three times higher than that of graphene on SiO_2. However, graphene/BN devices are troublesome to fabricate and are thus not ideal for industrial applications.

CHAPTER 4

TEMPERATURE DEPENDENT TRANSPORT PROPERTIES OF
THE PRISTINE GRAPHENE

The pristine graphene samples on SiO_2 substrate are fabricated by chemical vapor deposition on Cu foil, graphene transfer and hall bar patterning. Details of the fabrication procedures are discussed in Chapter 2. With these pristine graphene samples, temperature dependent transport properties are carried out by measuring the Hall effect from room temperature to 10 K.
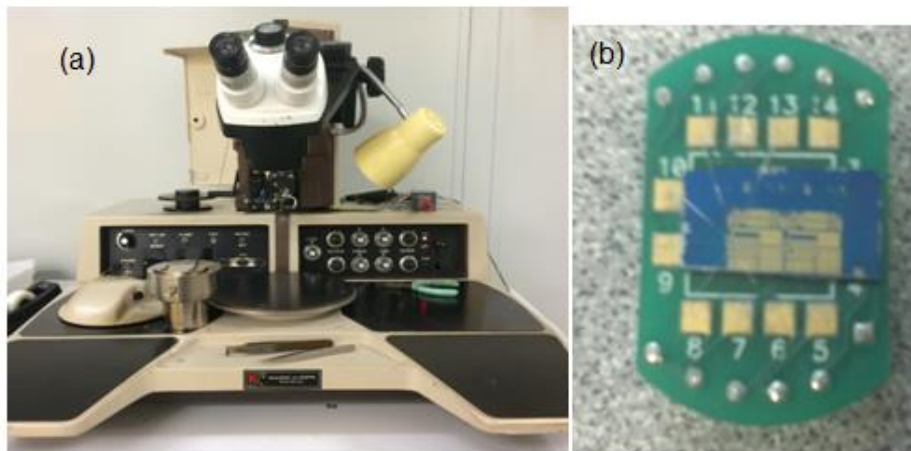
Figure 4.1 (a) Kulicke and Soffa Model 4123 wire bonder. (b) Wire bonded graphene sample with Hall bar devices on PPMS sample holder.

4.1 Experiment Setup

After the fabrication process, the devices are silver-painted onto a sample holder for Quantum Design Physical Property Measurement System (PPMS). Then the devices are wire bonded by Kulicke and Soffa Model 4123 wire bonder, as shown in Fig. 4.1.
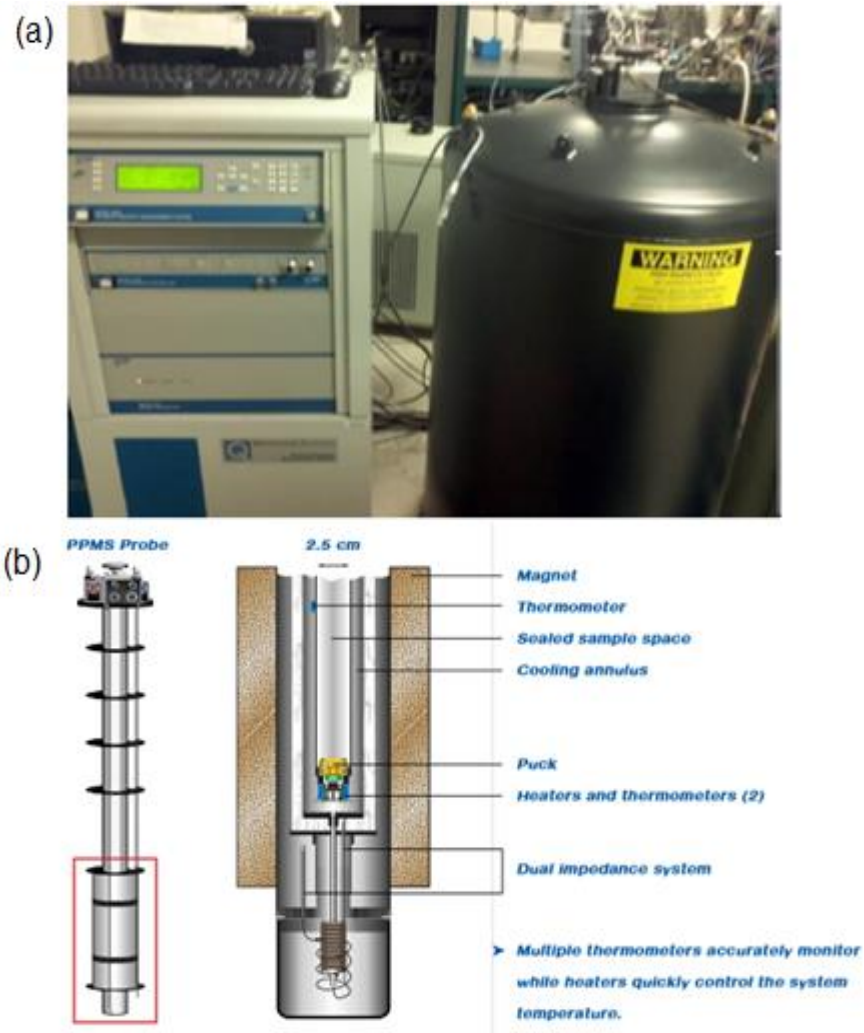
Figure 4.2 (a) Quantum Design PPMS Model 6000. (b) Schematic representation of the liquid helium cryostat in PPMS probe [78].

There is a liquid helium cryostat in PPMS probe, which is presented in Fi. 4.2 (b). The cryostat is able to be cooled down to $T = 4$ K and below in two steps using liquid nitrogen and liquid helium. Lower temperatures are achieved by reducing the vapor

43

pressure of helium by pumping. A superconducting magnet creates a magnetic field which can reach up to 9 T.
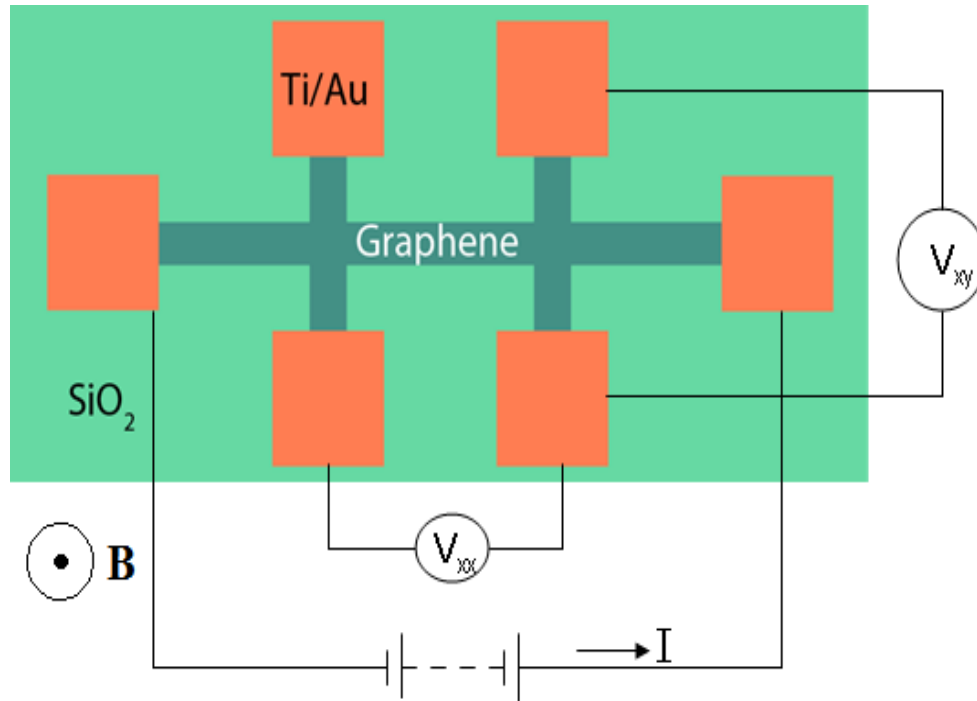
Figure 4.3 Electrical connections for Hall measurement and the direction of applied magnetic field.

The sample is placed at the bottom of the cryostat in such a way that the field is perpendicular to the plane of the graphene. Typical four-terminal method is used in our measurement, and the electrical connections for the measurement of resistivity and mobility are shown schematically in Fig. 4.3. A constant dc current was applied through the devices and the voltages V_{xx} and V_{xy} (also known as the Hall voltage V_H) were measured across the terminals when a magnetic field is turned on. This method avoids the contact resistance at the current injection points. The maximum magnetic field used in the experiment is 8 T in order to avoid potential problems caused by overloading the PPMS.

44

According to Eq. (3.8) and Eq. (3.9) and considering the fact that graphene is two-dimensional material, the carrier density p can be written as

$$p = \frac{IB}{qV_H} , \tag{4.1}$$

where I is the constant dc current, B is the magnetic field, and q is the electron charge. Then, the carrier mobility μ is expressed as

$$\mu = \frac{\sigma_{xx}V_H}{IB} , \tag{4.2}$$

where σ_{xx} is the conductivity along the current direction derived by V_{xx} and the device dimensions.

4.2 Results and Discussion

35 samples have been investigated from 300 K to 10 K. 34 of them showed the usual Hall effect, where the Hall Voltage kept increasing with the magnetic field. However, for one single layer graphene device, it exhibited quantum Hall effect when it was cooled down to 60 K, as plotted in Fig. 4.4 (a). This sample is labeled as QHE device for convenience.

4.2.1 Observation of Quantum Hall Effect

The Hall voltage V_{xy} of QHE device displays one plateau around 6.2 T, which is the precursor of the quantum Hall effect. At that point, electronic degrees of freedom in graphene are condensed into Landau levels [8]. The plateau value can be determined by the unconventional Landau level [79]:

$$V_{xy} = Ih / (4n+2)e^2 , \tag{4.3}$$

where h is the Planck constant, n is the Landau level index. For the plateau value shown in Fig. 4.4, n is equal to 5. This QHE device was further cooled down to 4 K, but no other

45

plateaus showed up. Stronger magnetic field is needed to be able to observe more step-like plateaus with lower index numbers of Landau levels.
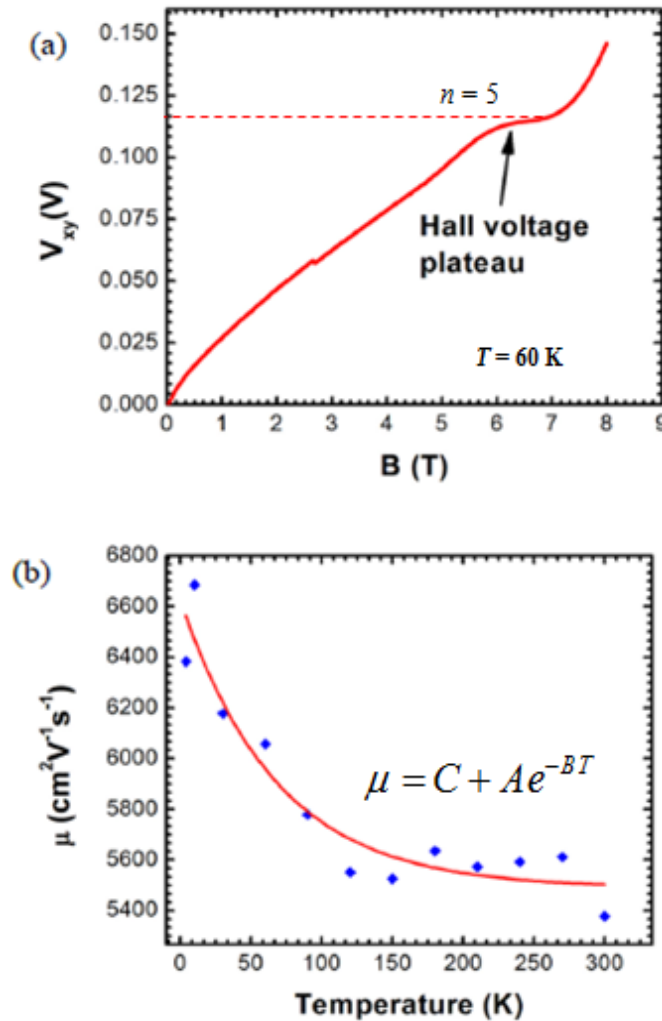
Figure 4.4 (a) Quantum Hall effect in QHE device at $T = 60$ K. The Hall voltage plateau value corresponds to Landau level index of 5. (b) Temperature dependence of Hall mobility μ (blue rectangles) in QHE device. The red line is the fitting of Eq. (4.4).

The observation of the quantum Hall effect is conditional on many factors. Firstly, very high-quality samples must be used in order to maximize the momentum scattering time τ_q of the electrons. Secondly, high magnetic fields B are needed in order for the

cyclotron period of the carriers to be much shorter than the scattering time τ_q. Equivalently, this means that the cyclotron frequency ω_c must be much higher than the broadening of the carrier energy levels: $\omega_c \tau_q >> 1$. Last but not the least, low temperature is required to satisfy that the thermal energy $k_B T$ is much less than the spacing the Landau levels: $k_B T << \hbar \omega_c$.

The PPMS in our lab can produce a relatively large magnetic field and reach the temperature as low as 2 K so that the most important factor to observe the quantum Hall effect of graphene is to have high-quality uniform single layer graphene which is lack of defects and impurities. Since there are a lot of chances to contaminate the graphene samples during the fabrication procedures, only one graphene device satisfies all the requirements list above.

4.2.2 Temperature Dependence of Carrier Density and Mobility

The charge carrier density and charge carrier mobility values were extracted from the Hall measurement from Eq. (4.1) and Eq. (4.2). The charge carrier density of $p \sim 10^{12}$ cm^{-2} and mobility $\mu \sim 2000$ cm^2 /Vs were found for most of our samples at room temperature. However, the QHE device has much higher mobility $\mu \sim 5400$ cm^2 /Vs at room temperature and 6600 cm^2 /Vs at 10 K, as shown in Fig. 4.4(b). The temperature dependence of carrier mobility μ can be expressed by the following equation:

$$\mu = C + Ae^{-kT}, \tag{4.4}$$

where A, k and C are the fitting parameters. In addition, its mobility decreases as temperature increases, especially when the temperature is below 120 K, indicating that the

QHE device is monolayer graphene and substrate surface polar phonon scattering is the dominant source of scattering.
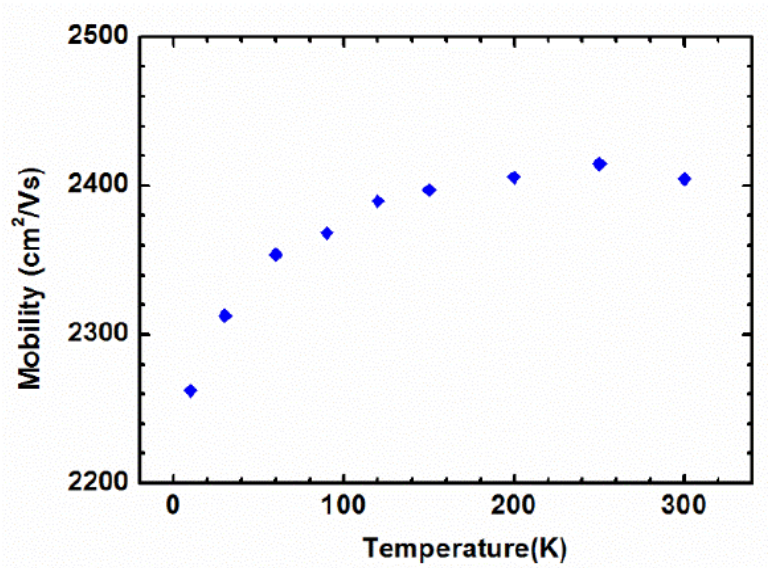
Figure 4.5 Temperature dependent mobility of a typical bilayer graphene sample.

Fig. 4.5 shows the temperature dependent mobility of a typical bilayer graphene sample exhibiting opposite trend compared to the QHE device. The mobility reduced from 2405 cm^2/Vs at room temperature to 2260 cm^2/Vs at 10 K, indicating that it is bilayer graphene and Coulomb scattering becomes the primary source of scattering. Our results are in good agreement with Ref. [68]. The different trends in the variation in the carrier mobility in monolayer and bilayer graphene can be explained by differences in their density of states and the additional screening of substrate surface polar phonon induced electrical field in bilayer graphene, which has been described in Section 3.4.1.

48

CHAPTER 5

EFFECT OF PALLADIUM HYDRIDE SURFACE FUNCTIONALIZATION ON GRAPHENE

5.1 Metal Surface Functionalization on Graphene

Due to its two dimensional (2D) nature, charge carriers in graphene are confined within one atomic layer thickness and its properties are easily influenced by the surrounding medium. Influenced properties due to surface effect can include electrical, chemical, optical, and mechanical properties. In addition to excellent material properties, the ability to form layered heterostructure with other lower dimensional materials, where the interface properties such as barrier height can be modulated, opens up a lot of possible devices and sensing applications. Since graphene properties can be easily influenced by surrounding medium, engineering its surface adds new functionality and is very attractive for device and sensing applications. Metal nano-particle (NP) functionalization of graphene is one such technique to not only change the doping but also facilitate sensing of analytes to which pristine graphene does not respond. For example, hydrogen, which is considered as a clean and renewable energy source, has drawn significant research interest around the world.

49

However, H_2 is odorless and highly flammable above 4 vol% in air [80], which leads to serious safety concern about its storage and usage. It is important to detect H_2 level and turn off equipment accordingly to avoid a dangerous explosion. Therefore, H_2 gas sensors for leakage detection are highly demanded in space and industrial applications. Although it has been reported that pristine graphene is insensitive to H_2 [26], noble metal surface functionalization on graphene has been used to fabricate high sensitivity graphene-based H_2 gas sensors [27-30].

Generally speaking, the sensitivity of graphene-based H_2 gas sensors is subject to two factors: (i) the sum of charge transferred from the metal hydrides, and (ii) the mobility and density of the charge carriers in graphene, since conductivity is proportional to the product of carrier mobility and density. The former relies upon the material properties and thickness of the functionalization layer, while the latter depends on the scattering caused by the functionalization layer [81,82] and substrate beneath the graphene [39]. Therefore, these two factors mentioned above limit the quality of graphene-based H_2 gas sensors. Although in all the amperometric sensing mechanism involves change in current transport, there has not been any study on change in transport properties such as mobility for analytes such as H_2 exposure. Understanding the effect of metal NP functionalization on these properties would improve the quality of graphene-based H_2 gas sensors and pave the path for new applications.

5.2 Palladium NP Functionalization

As mentioned in Section 2.3, only large size Hall bar devices were used to carry out Pd NP functionalization due to the difficulty of shadow mask alignment. After initial material and electrical characterization of the pristine graphene samples, 2 nm Pd was

50

deposited on the graphene channel region using shadow mask by electron beam evaporation at a base pressure of 10^{-6} Torr.
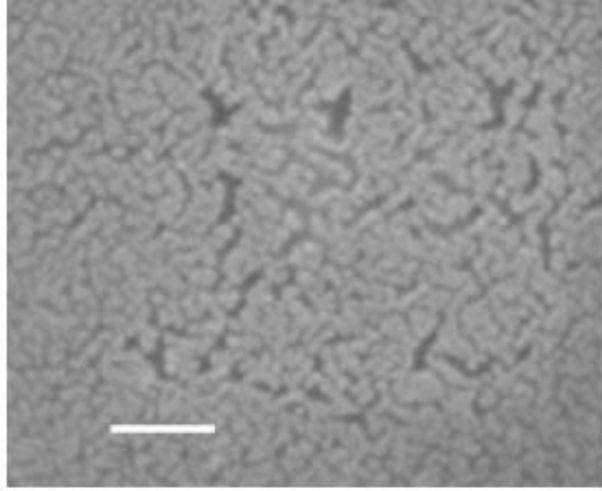
Figure 5.1 SEM image of 2 nm Pd-functionalized graphene.
The scale bar is 50 nm.

Fig. 5.1 captures the image of Pd grains on graphene in a high resolution scanning electron microscopy (SEM). Due to slow growth rate (~0.2 Å) and the short deposition time (~100 seconds for 2 nm), the growing Pd grains could not coalesce to form complete film coverage so that graphene was partially covered and still the current carrying channel.

5.3 Results and Discussion

Two samples were investigated after Pd NP functionalization, labeled as Sample A and Sample B.

5.3.1 Raman Characterization

Raman characterization was performed on Sample B before and after Pd deposition. Raman spectra for single layer graphene is shown again here in Fig. 5.2(a) to compare with bilayer graphene. Fig. 5.2(b) presents the Raman spectra of pristine and functionalized graphene. 2D/G ratio of 1.65 and 2D peak full width half maximum (FWSM) of ~34 cm^{-1}

51

indicates our sample is bilayer graphene [34]. Initial D/G peak intensity ratio is around 0.1, which does not show significant change after Pd NP deposition. No significant change in D/G ratio and peak position confirms that no degradation or other structural change happened after Pd NP functionalization of graphene on SiO_2 substrate.
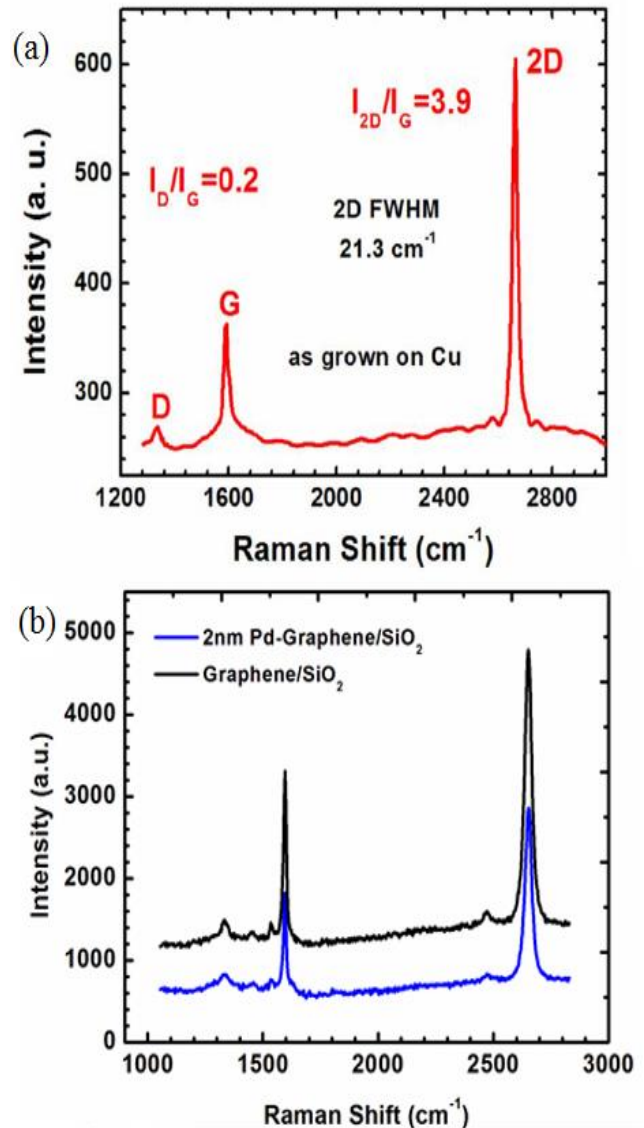
Figure 5.2 Raman spectra of (a) single layer graphene, and (b) bilayer graphene on SiO_2/Si before and after 2 nm Pd deposition.

5.3.2 Transport Measurement for Pd-functionalized Graphene
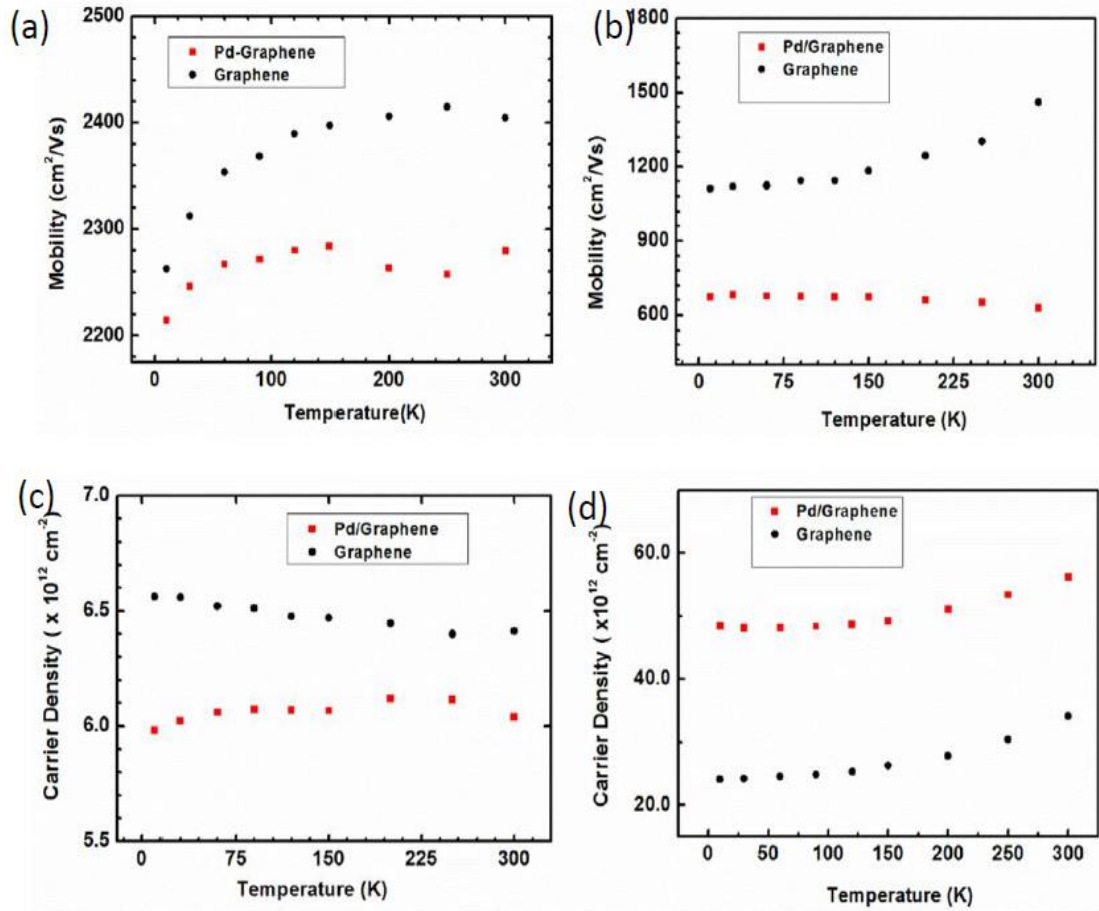
Figure 5.3 Temperature dependent mobility of bilayer graphene before and after 2 nm Pd deposition for (a) Sample A and (b) Sample B, and Carrier Density for (c) Sample A and (d) Sample B, respectively.

Afterwards, temperature dependence of the carrier mobility and density of the Pd-functionalized graphene were measured. Fig. 5.3 is showing the effect of 2 nm Pd deposition on graphene, changes in mobility and carrier density. In both samples mobility reduce after the Pd deposition, since additional Pd functionalization layer introduces another source of scattering as expected. However, in Sample A [Fig. 5.3(a)] mobility reduction is much less compared to Sample B [Fig. 5.3(b)]. Room temperature reduction

in mobility for Sample A is from 2405 to 2279 cm^2/Vs compared to a significant reduction from 1460 to 630 cm^2/Vs for Sample B, which is about 57% off.
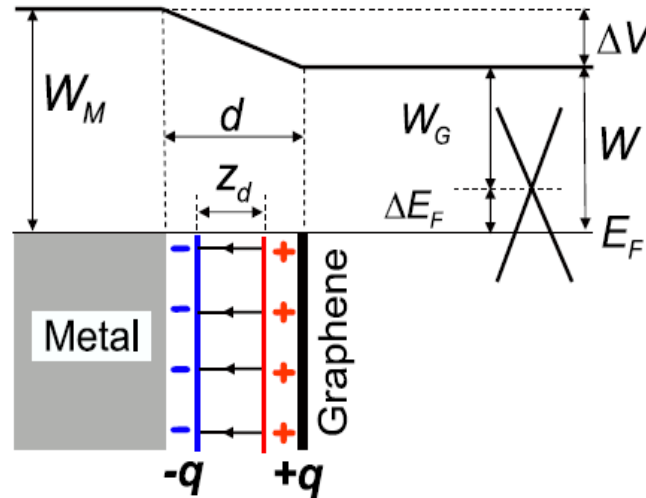
Figure 5.4 Schematic illustration of the model used to explain interface dipole and potential step formation at the graphene-metal interface [83].

With Pd NP, mobility in Sample A decreases as temperature decreases, following the trend of the pristine graphene with minor exception over the temperature range of 250 to 200 K [Fig. 5.3(a)], which is small considering the overall measurement temperature range. Like multilayer graphene, Coulomb scattering is the dominant scattering source in Sample A before and after Pd deposition. However, mobility in Sample B increases slightly about 7% from 630 to 672 cm^2/Vs as temperature decreases. Considering the observation of the significant reduction of mobility in Sample B mentioned above, Pd functionalization layer induced scattering becomes as important as Coulomb scattering so that Coulomb scattering is no longer the major scattering mechanism in Sample B with Pd NP. This can also explain why mobility drops about 57% for Sample B after Pd deposition, just like parallel resistors.

54

In addition, carrier density variations at different temperature for both samples are plotted in Fig. 5.3(c) and (d). Surprisingly the Pd NP induced doping is opposite for the two samples. For Sample A, room temperature hole density decreased slightly from 6.4×10^{12} to 6.0×10^{12} cm^{-2} and for Sample B, increased from 3.4×10^{13} to 5.6×10^{13} cm^{-2}, indicating n-type doping for the former and p-type doping for the later.

To explain this, one possible way is to apply the numerical and analytical model (as shown in Fig. 5.4) developed by Giovannetti et al. [83] for interaction between graphene and metal, such as Al, Ag, Cu, Au, and Pt which forms weak bonding with graphene while preserving its electronic structure. Although graphene electronic structure can be significantly altered by Pd (111), in our case, its thickness is 2 nm which does not form a continuous layer (forms grains of 20-30 nm as seen in Fig. 5.1) and any noticeable change has not been observed in Raman spectra shown in Fig. 5.2(b), the mentioned model can be employed for Pd NP as well.

Naively one would assume that graphene is doped with electrons if work function of graphene is larger than work function of metal ($W_G > W_M$) and doped with holes if work function of graphene is less than work function of metal ($W_G < W_M$). Considering higher work function of Pd compared to graphene, p doping can be easily expected. However, from numerical and analytical model in Ref. 83, nature of charge transfer depends on the separation distance between graphene and metal. It clearly demonstrates that the charge redistribution at the graphene-metal interface is not only the result of an electron transfer between the metal and the graphene levels originated from the difference in work function. There is also a contribution from the metal graphene chemical interaction. Graphene work function is preserved to its freestanding value of 4.5 eV only when graphene-metal distance

55

is greater than 4.2 Å, the potential due to metal graphene chemical interaction is very small and charge transfer depends only on the work function. For smaller distance, chemical interaction induced potential becomes significant which increases the effective graphene work function significantly, as for example, at the equilibrium distance of 3.3 Å, theoretically obtained W_G is 5.4 eV much higher than its freestanding value. Defining metal work function as W_M and $\Delta V(d)$ as the potential change generated by the metal-graphene chemical interaction, Fermi level shift in graphene $\Delta E_F(d)$ as a function of the graphene-metal surface distance d can be given by the following equation,

$$\Delta E_F(d) = W_M - \Delta V(d) - W_G \qquad (5.1)$$

The dependence of the Fermi level shift $\Delta E_F(d)$ on the metal-graphene separation d is mapped out in Fig. 5.5(a). For Pt which has highest work function, Fermi level shift is positive for all Pt-graphene separation and resultant doping in graphene is always p-type. For Al which has lowest work function, Fermi level shift is negative for all Al-graphene separation and resultant doping in graphene is always n-type. However, for the other three metals (Au, Cu, and Ag), doping type is decided by the metal-graphene separation. For example, the equilibrium separation for Cu is 3.4 Å. When Cu-graphene separation is greater than 3.4 Å, Fermi level shift is positive and resultant doping in graphene is p-type. When Cu-graphene separation is less than 3.4 Å, Fermi level shift is negative and resultant doping in graphene is n-type. This model [solid line in Fig. 5.5(a)] agrees with the density functional theory (DFT) results [dots in Fig. 5.5(a)].
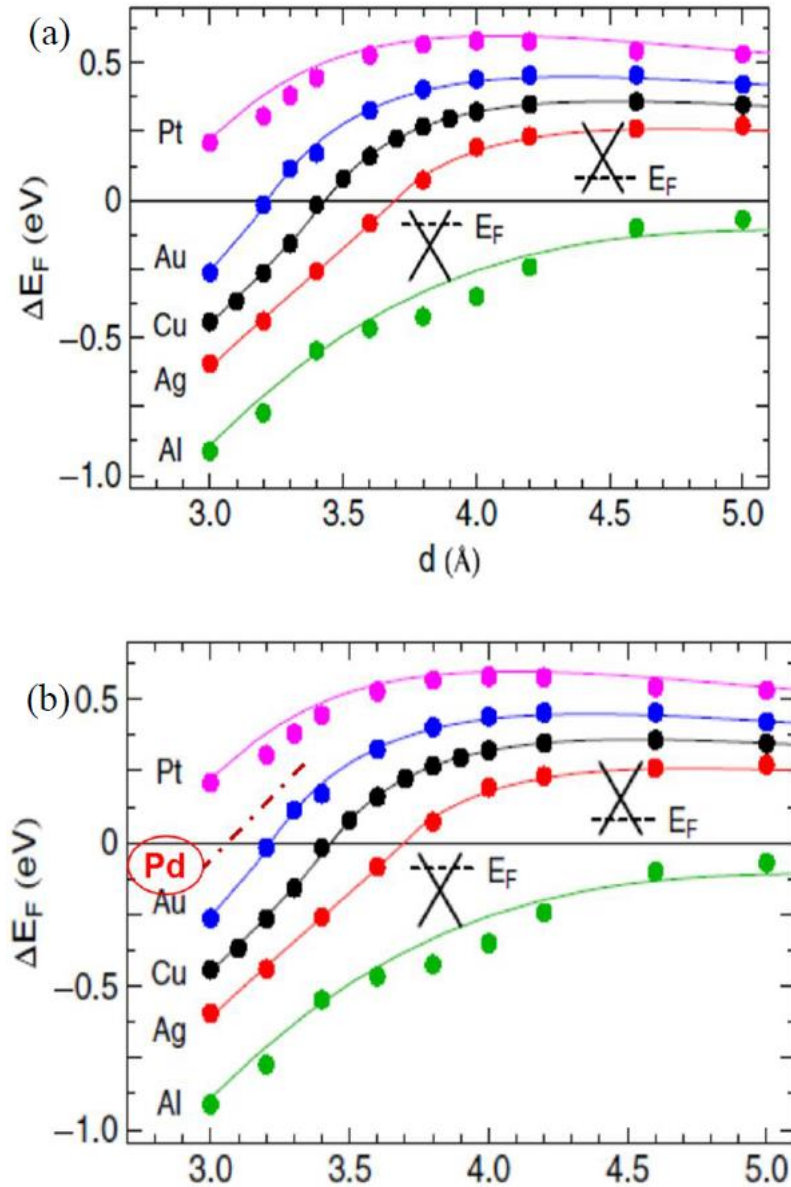
Figure 5.5 (a) Fermi level shifts $\Delta E_F(d)$ as a function of the graphene-metal surface distance d. The dots are obtained numerically from first-principles calculations based on DFT and the solid lines give the results obtained from analytical model [83]. (b) Predicted position is shown by the dashed line for Pd NP in between Pt and Au to explain the results obtained in this study for Pd NP induced doping of bilayer graphene.

Pd work function in this work is smaller than Pt, but larger than Au. And the trend for Pd might be in between Pt and Au as predicted in Fig. 5.5(b). For very small interaction distance d between Pd NP and graphene, Fermi level shift is negative and resultant doping

is n-type, reducing the p-doing of CVD graphene which has happened in Sample A. In Sample B, the Pd NP-graphene separation is larger than the equilibrium separation so that Fermi level shift is positive and resultant doping is p-type.

5.3.3 H₂ Sensing
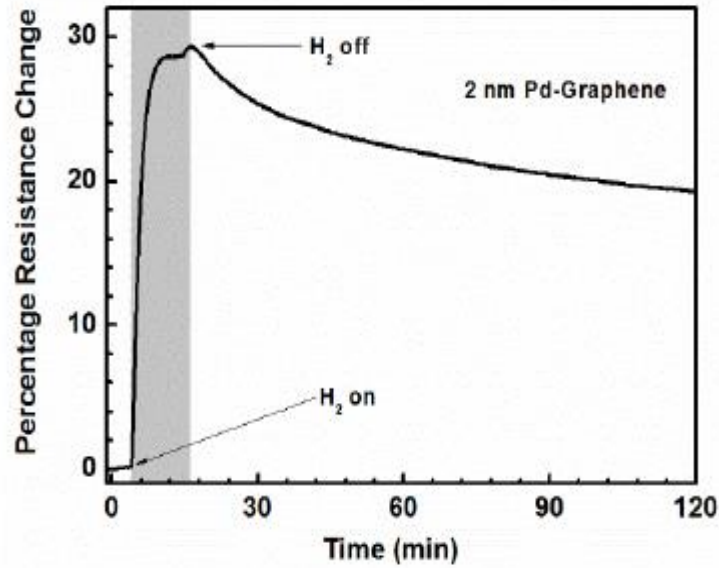
Figure 5.6 Effect of H₂ exposure on the resistance of Sample A with 2 nm Pd functionalization layer.

Next, H₂ sensing experiments are performed in the PPMS chamber at room temperature. 1000 ppm (parts per million) H₂ is flown into the chamber for about 12 minutes. Then, H₂ is turned off but N₂ is turned on. Fig. 5.6 shows the percentage resistance change $\Delta R / R$ of Sample A as a function of time at room temperature. The resistance change is defined as

$$\Delta R / R = (R_H - R) / R \times 100\% , \qquad (5.2)$$

where R and R_H are the resistance of the sample before and after exposure to H₂, respectively. It produces ∼ 29 % resistance change for 1000 ppm H₂, which is high

sensitivity for the graphene-based H_2 sensors compared to the previous reports [27,28]. Here the recovery is slow due to only N_2 exposure instead of air which contains O_2 and helps fast recovery.

5.3.4 Transport Measurement for PdH$_x$-functionalized Graphene

Subsequently, with the presence of H_2, transport properties of the Pd-functionalized graphene are measured from room temperature to 10 K. 1000 ppm H_2 is flown for enough time to stabilize the conductivity of samples at each different temperature. Then Hall measurements are performed and carrier density and mobility are extracted.

Fig. 5.7(a) shows the carrier mobility of the pristine graphene (black dots), the Pd-functionalized graphene without H_2 (red squares), and the Pd-functionalized graphenen with H_2 (blue triangles) as a function of temperature for Sample A. A huge enhancement of the mobility has been observed after the exposure to H_2. At room temperature, the mobility increases about 49%, from 2279.8 cm^2/Vs to 3394.5 cm^2/Vs after H_2 exposure and the enhancement is even larger at low temperature. Another important point to note regarding the temperature dependence of the mobility for H_2 exposure, mobility increases with the decrease in temperature, which is completely opposite without H_2 exposure. Similar trend has been observed for monolayer graphene [Fig. 4.4(b)], which originates when surface phonon scattering is the dominant mechanism influencing the electrical transport. Considering that Coulomb scattering is the dominant scattering mechanism in Sample A before and after Pd deposition, this indicates that the dominant transport mechanism for H_2 exposed Pd-functionalized bilayer graphene switches from Coulomb scattering to surface optical phonon scattering.

59

Figure 5.7 Effect of H_2 exposure on (a) mobility and (b) carrier density for Sample A over the temperature range of 300 to 10 K.

This change can be explained by the formation of PdH_x on graphene surface which has high dielectric constant [84] and higher resistivity compared to metallic Pd [85]. When H_2 molecule interacts with Pd NP, it dissociates into atomic hydrogen and forms PdH_x [86], which has an electrical dipole structure resulting in electron accumulation at the interface with graphene, and also reduces the hole density in graphene from 6.0×10^{12} to 2.4×10^{12} cm^{-2} at room temperature [as shown in Fig 5.7(b)].

In addition to reduction of carrier concentration by PdH_x formation, its high dielectric constant also helps in screening Columbic scattering, essentially resulting in

mobility enhancement. The fact that dielectric constant value of PdH_x is larger than both Pd and air makes the sample a sandwich structure of dielectric/graphene/dielectric.
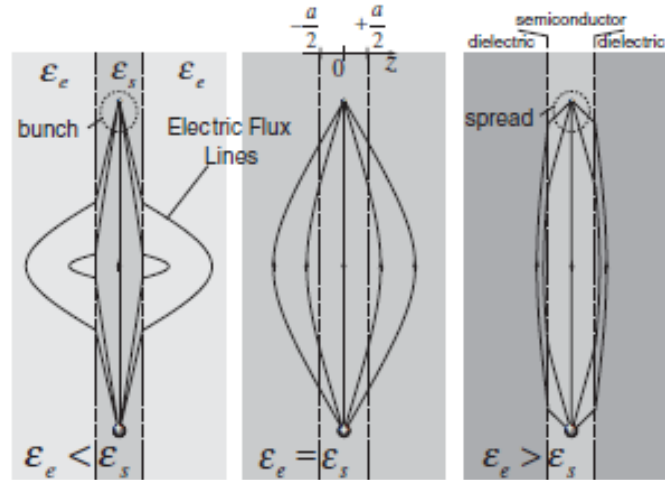
Figure 5.8 Electric flux lines originating from a fixed ionized impurity and terminating on a mobile electron, and the effect of the dielectric environment [87].

This type of structure has been proposed by D. Jena and A. Konar to achieve large improvements in carrier mobility in 2- and 1-dimensional semiconductor nanostructures in 2007 [87]. Considering in a thin 2D semiconductor membrane of thickness a, a point charge e is located at $(0, 0, z_0)$, as seen in Fig. 5.8. By the method of image charges, the unscreened potential due to the Coulomb scattering experienced by a mobile electron inside the membrane is found to be dominated by the dielectric constant mismatch between the dielectrics and the semiconducting membrane. The flux lines in Fig. 5.8 bunch closer inside the semiconductor layer if $\varepsilon_e < \varepsilon_s$, and spread farther apart if $\varepsilon_e > \varepsilon_s$, thus enhancing Coulomb interaction in the former case and damping it in the latter. By coating 2D semiconductor nanostructures with high-κ dielectrics, Coulomb scattering inside the

61

semiconductor can be dramatically damped so that the mobility improves as much as an order of magnitude for GaAs.
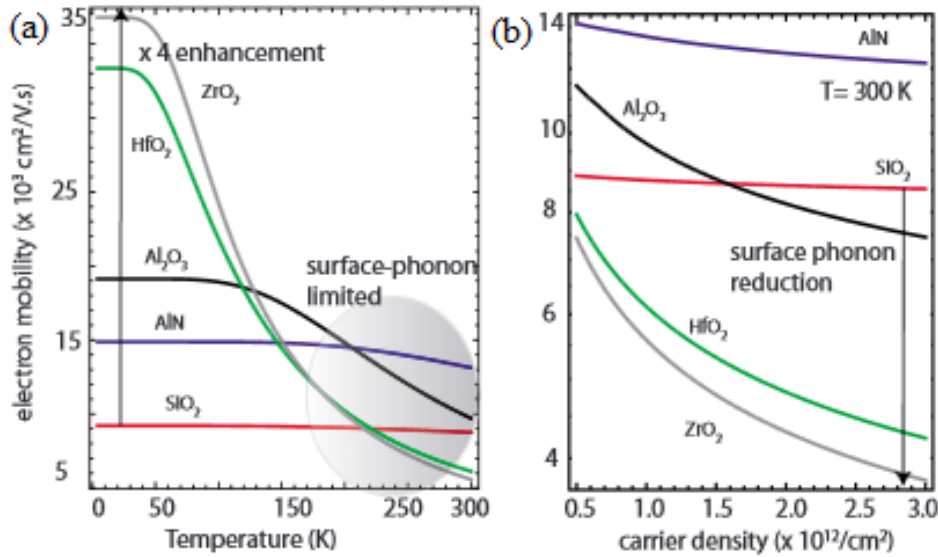
Figure 5.9 (a) Mobility in graphene as a function of temperature on different gate dielectrics at carrier density $n = 10^{12}$ cm^{-2}. (b) Mobility as a function of carrier density on different gate dielectrics at $T = 300$ K [88].

In 2010, Konar's group further investigated the effect of various gate dielectrics on mobility in air/single-layer graphene/dielectric structure [88]. It is found that though high-κ dielectrics can strongly reduce Coulombic scattering by dielectric screening, high-κ dielectrics lead to enhanced surface optical phonon scattering at room temperature due to remote optical phonon coupling between electrons in the channel and polar vibrations in the dielectric. Fig. 5.9(a) shows the temperature-dependent carrier mobility for graphene on different dielectrics. Indeed, at low temperature, mobility can be improved by a factor of 4 (gray curve in Fig. 5.9) by choosing ZrO$_2$ as the dielectric gate. But at room temperature, mobility values are reduced for all dielectrics due to enhanced surface optical phonon scattering. The carrier density dependence of carrier mobility at $T = 300$ K is

mapped out in Fig. 5.9(b). Numerical fittings show that mobility varies with carrier density following the relationship

$$\mu(n) \sim n^{-\alpha}, \tag{5.3}$$
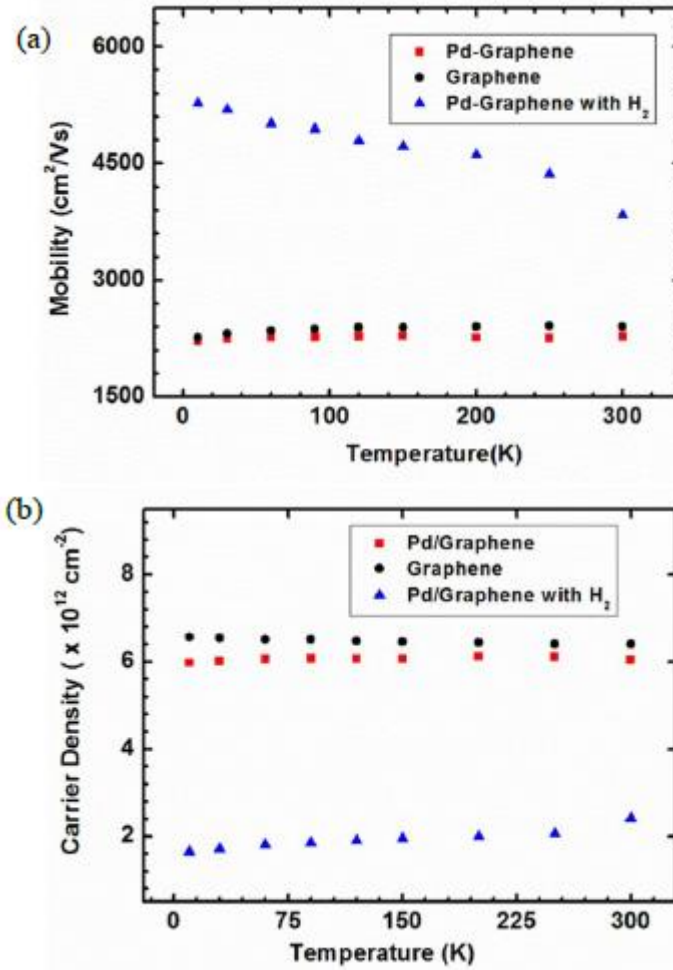
where the exponent α lies between 0.3 to 0.4.
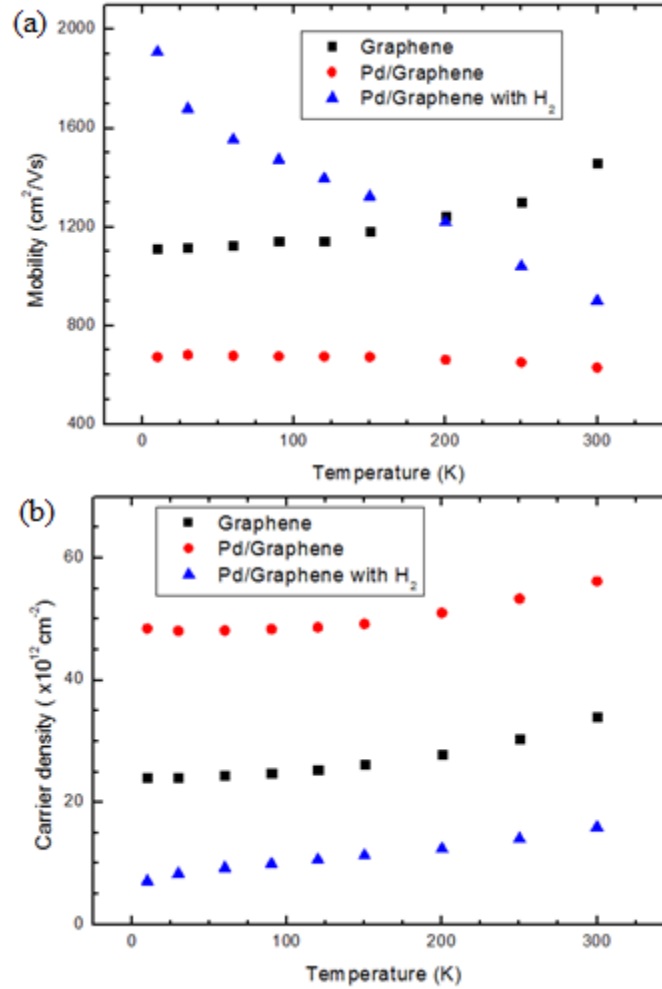
Figure 5.10 Effect of H_2 exposure on (a) mobility and (b) carrier density for Sample B over the temperature range of 300 to 10 K.

Although the structure of our samples is a little bit different from the discussed ones in Ref. [87] and [88], the damping of Coulomb scattering and the mobility enhancement over all temperature range have been observed in both samples in spite of different doping

type after Pd deposition. As shown in Fig. 5.10(a), for Sample B, room temperature mobility increases from 630 to 902 cm^2/Vs with H_2 exposure, which further increases to 1910 cm^2/Vs at 10 K. Similarly, Coulomb scattering is no longer dominant and surface optical phonon scattering becomes the most important one. Experimental mobility enhancement in graphene by depositing conventional high-κ dielectrics such as HfO_2 and Al_2O_3 [89] has also been reported.

From Fig. 5.10(b), the carrier density reduces 5.6×10^{13} to 1.6×10^{13} cm^{-2} at room temperature and further down to 7.1×10^{12} cm^{-2} at 10 K. As discussed before, PdH_x forms a dipole where its negatively charged part is at the interface with graphene, neutralizing the holes in graphene. Therefore, the hole density of the PdH_x-functionalized graphene is much lower than the one of the Pd-functionalized graphene.
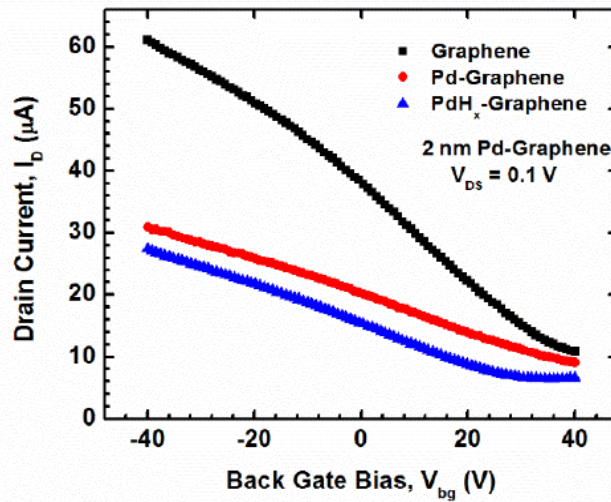
Figure 5.11 Back Gated transfer characteristics of bilayer graphene at room temperature for three different conditions.

Finally, room temperature back gated measurements of bilayer graphene device fabricated next to the Hall bar on Sample B have been carried out at three different conditions, as shown in Fig. 5.11. Initially field effect mobility of graphene is calculated

64

to be 1735 cm^2/Vs and current minima point is close to 40 V. After 2 nm Pd deposition, mobility reduces to 652 cm^2/Vs and from the almost linear nature of current decrease, it can be estimated that the Dirac point shifts to higher positive voltage. This higher Dirac voltage compared to that of before Pd deposition indicates that Pd NP increases graphene's p-type doping resulting in higher residual carrier density.

After H_2 exposure, although the Dirac point shifts towards left, mobility does not show significant increase. The Dirac point shift towards lower positive voltage means PdH_x reduces hole concentration in graphene. With the decrease in carrier concentration, a little improvement in mobility has been observed as visible from the slightly higher slope of the blue line. It can be attributed to PdH_x dipole. The electric field from the dipole most likely influences the moving charge carriers in a similar way to that of a polar dielectric with large dielectric constant, where the optical phonon couples with the carriers in the channel and results in scattering which tries to offset the mobility enhancement due to dielectric screening induced reduction in Coulomb scattering. Hence, this might be the reason for the slightly increase in mobility after H_2 exposure at room temperature. Due to some unknown reasons, there always exists a current leaking problem in the gate when back gated measurement is performed in PPMS at low temperature. We have not confirmed the mobility enhancement at low temperature from back gated characterization. But from the Hall mobility variation with temperature, we can expect that, filed effect mobility with H_2 exposure would also increase at low temperature.

CHAPTER 6

CONCLUSIONS AND FUTURE WORK

6.1 Summary

This dissertation primarily focused on the temperature dependent transport properties of Pd nanoparticle functionalized and hydrogenated CVD grown graphene. Hall effect measurements have been carried out to investigate transport properties and scattering mechanisms in graphene, Pd/graphene, and PdH_x/graphene. Interestingly, the mobility enhancement has been observed in the PdH_x/graphene samples over a wide temperature range of 300 to 10 K.

In Chapter 1, electronic structure of graphene is firstly introduced. Due to its stimulating electrical, optical, mechanical and numerous other interesting properties, graphene has been extensively studied over the last decade. For reliable and successful development of graphene based devices, availability of large area, uniform, and quality graphene film is highly desirable. Mechanical exfoliation, thermal decomposition of SiC, and chemical vapor deposition are commonly used techniques to produce good quality graphene.

Chapter 2 started with CVD graphene growth steps including substrate copper substrate preparation, annealing and final growth phase, etc. Raman spectroscopy

66

characterization confirms the good quality of graphene made in our lab. Fabrication process for different size of hall bar samples, including details of graphene transfer on arbitrary substrate utilizing PMMA assisted transfer technique, photoresist lithography, metal contact pad deposition, and oxygen plasma etching, has been developed for CVD grown graphene.

After the discussion of fundamental details of Hall effect, transport properties and scattering mechanisms in monolayer graphene and multilayer graphene from previous literatures have been reviewed in Chapter 3. In particular, graphene shows remarkable high carrier mobility up to 200,000 cm^2/Vs in suspended graphene. However, this value is extremely reduced to only a few thousand cm^2/Vs in supported graphene on SiO_2 or SiC substrates, due to different sources of scattering.

In Chapter 4, we investigate temperature dependent carrier mobility and carrier density of 35 pristine graphene samples. 34 out of 35 samples show normal Hall effect, while one specific sample exhibits quantum Hall effect (QHE) with one step-like plateau in Hall voltage around $B = 6.2$ T when it was cooled down to 60 K. In those 34 pristine graphene samples, the Hall mobility decreases with temperature decreases, indicating that the mobility is dominated by Coulomb scattering and graphene is bilayer. However, the QHE device has much higher mobility ~ 5400 cm^2/Vs at room temperature and its mobility decreases as temperature increases, suggesting that substrate surface polar phonon scattering is the main source of scattering and graphene is monolayer.

Metal nano-particle (NP) functionalization of graphene is one technique to not only change the doping but also facilitate sensing of analytes to which pristine graphene does not respond. By depositing a thin layer of catalytically active noble metals (such as Pd and

67

Pt) on the surface of graphene, charges can transfer between graphene and the metal hydride formed in the presence of H_2, realizing H_2 detection. After 2 nm Pd deposition on the surface of graphene to facilitate H_2 detection, temperature dependent carrier mobility and carrier density have been reinvestigated in the first part of Chapter 5. The Pd functionalized layer reduces mobility by inducing another source of scattering. However, the mobility enhancement has been observed in the Pd NP decorated graphene samples with H_2 exposure. Simultaneously, Coulomb scattering is damped and the dominant scattering mechanism switches to surface optical phonon scattering. The improvement in transport property and change in scattering mechanism can be attributed to hydrogenation of Pd, which results in thin layer of polar and insulating PdH_x with high dielectric constant. The nature of temperature dependent Hall mobility of Pd NP decorated graphene after H_2 exposure completely agrees with the theoretical prediction and experimental demonstration of carrier mobility enhancement in semiconductor nanostructures by high-κ dielectric engineering.

6.2 Future Work

Temperature dependent transport properties study can be further extended by varying the thickness of Pd, depositing other similar material such as Pt and Au, and comparison between the metals. In the dissertation, only 2 nm Pd has been deposited on graphene and investigated by Hall effect measurement. We can try different thickness of Pd to have a comprehensive study of the thickness dependence on carrier density and mobility. With different thickness of Pd, PdH_x/graphene samples may show different amount of mobility enhancement and we may find the maximum mobility enhancement at a certain Pd thickness. As mentioned above, catalytically active noble metal surface

functionalization method has been widely utilized to obtain high sensitivity graphene-based H_2 gas sensors [27-30]. Pt, Pd and Au are the possible candidates of noble metal which we can coat on the surface of graphene to facilitate H_2 sensing. Graphene samples with Pt or Au functionalization layer can be fabricated and tested. Comparisons between the effect of different metals on sensitivity of H_2 detection and transport properties before and after H_2 exposure are the potential topics. Furthermore, these types of study can be carried out for other 2D materials such as MoS_2, WSe_2, etc.

Due to the two opposite condition of high dielectric constant to reduce Coulomb scattering and high optical phonon frequency to reduce surface optical phonon scattering, we need a substrate which can satisfy both the conditions. In addition, Coulomb and short-range scattering limited carrier mobility in bilayer graphene is inversely proportional to the square of the effective mass. Thus, due to heavier effective mass with the number of graphene layer increase, for the same impurity concentration, Coulomb and short-range scattering limited mobility degradation is higher [68]. Hence, to improve the transport properties including mobility in multilayer graphene, it is imperative to reduce the impurity concentration either by process optimization or substrate/dielectric engineering. Considering the discussion in Section 3.4 about hexagonal Baron Nitride (hBN) which reduces the residual charge impurities in graphene eliminating the requirement of high dielectric constant and meanwhile has high optical phonon frequency close to that of graphene, it appears to be better substrate for graphene applications. Graphene on hBN has high mobility and hence expected to increase the sensitivity and quality of graphene devices. The improvement in Hall mobility for epitaxial graphene with CVD grown hBN top dielectric compared to HfO_2 [90,91] also supports this proposition. Therefore, hBN is

69

the top substrate candidate for graphene to reach higher mobility and better device performance if we can overcome the difficulty in the fabrication process.

REFERENCES

[1] K. S. Novoselov, A. K. Geim, S. V. Morozov, D. Jiang, Y. Zhang, S. V. Dubonos, I. V. Grigorieva, and A. A. Firsov, "Electric field effect in atomically thin carbon film," *Science* **306**, 666 (2004).

[2] C. Lee, X. Wei, J. W. Kyser, and J. Hone, "Measurement of the elastic properties and intrinsic strength of monolayer graphene," *Science* **321**, 385 (2008).

[3] R. R. Nair, P. Blake, A. N. Grigorenko, K. S. Novoselov, T. J. Booth, T. Stauber, N. M. R. Peres, and A. K. Geim, "Fine structure constant defines visual transparency of graphene," *Science* **320**, 1308 (2008).

[4] S. V. Morozov, K. S. Novoselov, M. I. Katsnelson, F. Schedin, D. C. Elias, J. A. Jaszczak, and A. K. Geim, "Giant intrinsic carrier mobilities in graphene and its bilayer," *Physical Review Letters* **100**, 016602 (2008).

[5] J. Chen, C. Jang, S. Xiao, M. Ishigami and M. S. Fuhrer, "Intrinsic and extrinsic performance limits of graphene devices on SiO_2," *Nature Nanotechnology* **3**, 206 (2008).

[6] D. R. Cooper, B. D'Anjou, N. Ghattamaneni, B. Harack, M. Hilke, A. Horth, N. Majlis, M. Massicotte, L. Vandsburger, E. Whiteway, and V. Yu, "Experimental review of graphene," *ISRN Condensed Matter Physics* **2012**, 501686 (2012).

[7] P. R. Wallace, "The band theory of graphite," *Physical Review* **71**, 622 (1947).

[8]   A. H. C. Neto, F. Guinea, N. M. R. Peres, K. S. Novoselov, and A. K. Geim, "The electronic properties of graphene," *Reviews of Modern Physics* **81**, 109 (2009).

[9]   A. K. Geim, "Graphene: status and prospects," *Science* **324**, 5934 (2009).

[10] C. Berger, Z. Song, T. Li et al., "Ultrathin epitaxial graphite: 2D electron gas properties and a route towards graphene based nanoelectronics," *Journal of Physical Chemistry B* **108**, 19912 (2004).

[11] S. Shivaraman, M. V. S. Chandrashekhar, J. J. Boeckl, and M. G. Spencer, "Thickness estimation of epitaxial graphene on SiC using attenuation of substrate raman intensity," *Journal of Electronic Materials* **38**, 725 (2009)

[12] X. Li, W. Cai, J. An et al., "Large-area synthesis of high-quality and uniform graphene films on copper foils," *Science* **324**, 1312 (2009).

[13] S. Bae, H. Kim, Y. Lee et al., "Roll-to-roll production of 30-inch graphene films for transparent electrodes," *Nature Nanotechnology* **5**, 578 (2010).

[14] C. Mattevi, H. Kim, M. Chhowalla, "A review of chemical vapor deposition of graphene on copper," *Journal of Materials Chemistry* **21**, 3324 (2011).

[15] A. C. Ferrari, F. Bonaccorso, V. Fal'ko et al., "Science and technology roadmap for graphene, related two-dimensional crystal, and hybrid system," *Nanoscale* **7**, 4598 (2015).

[16] Y. Lin, P. Avouris, "Strong suppression of electrical noise in bilayer graphene nanodevices," *Nano letters* **8**, 2119 (2008).

[17] F. Schedin, A. K. Geim, S. V. Morozov, E.W. Hill, P. Blake, M. I. Katsnelson, and K. S. Novoselov, "Detection of individual gas molecules absorbed on graphene," *Nature Materials* **6**, 652 (2007).

[18] P. E. Sheehan and L. J. Whitman, "Detection limits for nanoscale biosensors," *Nano Letters* **5**, 803 (2005).

[19] G. H. Lu, L. E. Ocola, and J. H. Chen, "Reduced graphene oxide for room–temperature gas sensors," *Nanotechnology* **20,** 445502 (2009).

[20] H. Y. Jeong, D. S. Lee, H. K. Choi, D. H. Lee, J. E. Kim, J. Y. Lee, W. J. Lee, S. O. Kim, and S. Y. Choi, "Flexible room-temperature NO_2 gas sensor based on carbon nanotubes/reduced graphene hybrid films," *Applied Physics Letters* **96,** 213105 (2010).

[21] G. H. Lu, L. E. Ocola, and J. H. Chen, "Gas detection using low-temperature reduced graphene oxide sheets," *Applied Physics Letters* **94,** 08311 (2009).

[22] V. Dua, S. P. Surwade, S. Ammu, S. R. Agnihotra, S. Jain, K. E. Roberts, S. Park, R. S. Ruoff, and S. K. Manohar, "All-organic vapor sensor using inkjet-printed reduced graphene oxide*,*" *Angewandte Chemie International Edition* **49,** 2154 (2010).

[23] J. D. Fowler, M. J. Allen, V. C. Tung, Y. Yang, R. B. Kaner, and B. H. Weiller, "Practical chemical sensors from chemically derived graphene," *ACS Nano* **3,** 301(2009).

[24] Md. W. K. Nomani, R. Shishir, M. Qazi, D. Diwan, V. B. Shields, M. G. Spencer, G. S. Tompa, N. M. Sbrockey, and G. Koley, "Highly sensitive and selective detection of NO_2 using epitaxial graphene on 6H-SiC," *Sensors and Actuators B: Chemical* **150,** 301 (2010).

[25] A. K. Singh, M. A. Uddin, J. T. Tolson, H. Maire-Afeli, N. Sbrockey, G. S. Tompa, M. G. Spencer, T. Vogt, T. S. Sudarshan, and G. Koley, "Electrically tunable molecular doping of graphene," *Applied Physics Letters* **102**, 043101 (2013).

73

[26] R. S. Sundaram, C. Gomez-Navarro, K. Balasubramanian, M. Burghard, and K. Kern, "Electrochemical modification of graphene," *Advanced Materials* **20**, 3050 (2008).

[27] W. Wu, Z. Liu, L. A. Jauregui, Q. Yu, R. Pillai, H. Cao, J. Bao, Y. P. Chen, and S. S. Pei, "Wafer-scale synthesis of graphene by chemical vapor deposition and its application in hydrogen sensing," *Sensors and Actuators B: Chemical* **150**, 296 (2010).

[28] B. H. Chu, C. F. Lo, J. Nicolosi, C. Y. Chang, V. Chen, W. Strupinski, S. J. Pearton, and F. Ren, "Hydrogen detection using platinum coated graphene grown on SiC," *Sensors and Actuators B: Chemical* **157**, 500 (2011).

[29] J. L. Johnson, A. Behnam, S. J. Pearton, and A. Ural, " Hydrogen sensing using Pd-functionalized multi-layer graphene nanoribbon networks," *Advanced Materials* **22**, 4877 (2010).

[30] M. A. Uddin, A. K. Singh, T. S. Sudarshan, and G. Koley, "Functionalized graphene/ silicon chemi-diode H_2 sensor with tunable sensitivity," *Nanotechnology* **25**, 125501 (2014).

[31] Y. Ren, S. Chen, W. Cai, Y, Zhu, C, Zhu, and R. S. Ruoff, "Controlling the electrical properties of graphene by in situ metal deposition," *Applied Physics Letters* **97**, 053107 (2010).

[32] J. L. Johnson, A. Behnam, Y. An, S. J. Pearton, and A. Ural, "Experimental study if graphitic nanoribbon films for ammonia sensing," *Journal of Applied Physics* **109**, 124301 (2011).

[33] D. M. Schaadt, B. Feng, and E. T. Yu, "Enhanced semiconductor optical absorption via surface plasmon excitation in metal nanoparticles," *Applied Physics Letters* **86**, 063106 (2005).

[34] A. C. Ferrari, J. C. Meyer, V. Scardaci, C. Casiraghi, M. Lazzeri, F. Mauri, S. Piscanec, D. Jiang, K. S. Novoselov, S. Roth, and A. K. Geim, "Raman spectrum of graphene and graphene layers," *Physical Review Letters* **97**, 187401 (2006).

[35] S. Berciaud, S. Ryu, L. E. Brus, and T. F. Heinz, "Probing the intrinsic properties of exfoliated graphene: Raman spectroscopy of free-standing monolayers," *Nano Letters* **9**, 346 (2009).

[36] A. C. Ferrari and D. M. Basko, "Raman spectroscopy as a versatile tool for studying the properties of graphene," *Nature Nanotechnology* **8**, 235 (2013).

[37] L. M. Malard, M. A. Pimenta, G. Dresselhaus, and M. S. Dresselhaus, "Raman spectroscopy in graphene," *Physics Reports* **473**, 51 (2009).

[38] A. C. Ferrari, " Raman spectroscopy of graphene and graphite: disorder, electron-phonon coupling, doping and nonadiabatic effects," *Solid State Communications* **143**, 47 (2007).

[39] J. Chan, A. Venugopal, A. Pirkle, S. McDonnell, D. Hinojos, C. W. Magnuson, R. S. Ruoff, L. Colombo, R. M. Wallace, and E. M. Vogel, "Reducing extrinsic performance-limiting factors in graphene growth by chemical vapor deposition," *ACS Nano* **6**, 3324 (2012).

[40] E. H. Hall, "On a new action of the magnet on electric currents," *American Journal of Mathematics* **2**, 287 (1879).

[41] K. S. Novoselov, A. K. Geim, S. V. Morozov, D. Jiang, M. I. Katsnelson, I. V. Grigorieva, S. V. Dubonos, and A. A. Firsov, "Two-dimensional gas of massless Dirac fermions in graphene," *Nature* **438**, 197 (2005).

[42] K. V. Emtsev, A. Bostwick, H. Horn et al., "Towards wafer-size graphene layers by atmospheric pressure graphitization of silicon carbide," *Nature Materials* **8**, 203 (2009).

[43] Z. Y. Juang, C. Y. Wu, C. W. Lo et al., "Synthesis of graphene on silicon carbide substrates at low temperature," *Carbon* **47**, 2026 (2009).

[44] X. Li, C. W. Magnuson, A. Venugopal et al., "Graphene films with large domain size by a two-step chemical vapor deposition process," *Nano letters* **10**, 4328 (2010).

[45] S. Lee, K. Lee, and Z. Zhong, "Wafer scale homogeneous bilayer graphene films by chemical vapor deposition," *Nano letters* **10**, 4702 (2010).

[46] K. Watanabu, T. Taniguchi, and H. Kanda, "Direct-bandgap properties and evidence for ultraviolet lasing of hexagonal boron nitride single crystal," *Nature Materials* **3**, 404 (2004).

[47] J. N. Coleman, M. Lotya, A. O'Neill et al., "Two-dimensional nanosheets produced by liquid exfoliation of layered materials," *Science* **331**, 568 (2011).

[48] P. Joensen, R. F. Frindt, and S. R. Morrison, "Single-layer MoS_2," *Materials Research Bulletin* **21**, 457 (1986).

[49] Z. Li, C. H. Lui, E. Cappelluti, L. Benfatto, K. F. Mak, G. L. Carr, J. Shan and T. F. Heinz, "Structure-dependent Fano resonances in the infrared spectra of phonons in few-layer graphene," *Physical Review Letters* **108**, 156801 (2012).

[50] *http://hyperphysics.phy-astr.gsu.edu/hbase/magnetic/hall.html*

[51] Y. H. Wu, T. Yu, and Z. X. Shen, "Two-dimensional carbon nanostructures: Fundamental properties, synthesis, characterization, and potential applications," *Journal of Applied Physics* **108**, 071301 (2010).

[52] A. K. Geim and K. S. Novoselov, "The rise of graphene," *Nature Material* **6**, 183 (2007).

[53] V. E. Dorgan, M. H. Bae, and E. Pop, "Mobility and saturation velocity in graphene on SiO$_2$," *Applied Physics Letters* **97**, 082112 (2010).

[54] F. Giannazzo, V. Raineri, and E. Rimini, "Transport properties of graphene with nanoscale lateral resolution," *Scanning Probe Microscopy in Nanoscience and Nanotechnology* **2**, 247 (2010).

[55] K. I. Bolotin, K. J. Sikes, J. Hone, H. L. Stormer, and P. Kim, "Temperature-dependent transport in suspended graphene," *Physical Review Letters* **101**, 096802 (2008).

[56] J. H. Chen, W. G. Cullen, C. Jang, M. S. Fuhrer, and E. D. Williams, "Defect scattering in graphene," *Physical Review Letters* **102**, 236805 (2009).

[57] J. H. Chen, C. Jang, S. Adam, M. S. Fuhrer, E. D. Williams, and M. Ishigami, "Charged-impurity scattering in graphene," *Nature Physics* **4**, 377 (2008).

[58] Y. Zhang, V. W. Brar, C. Girit, A. Zettl, and M. F. Crommie, " Origin of spatial charge inhomogeneity in graphene," *Nature Physics* **5**, 722 (2009).

[59] M. I. Katsnelson, and A. K. Geim, "Electron scattering on microscopic corrugations in graphene," *Philosophical Transactions of the Royal Society A* **366**, 195 (2008).

[60] N. M. R. Peres, "The transport properties of graphene," *Journal of Physics Condensed Matter* **21**, 32 (2009).

[61] D. Das Sarma, S. Adam, E. H. Hwang, and E. Rossi, "Electronic transport in two-dimensional graphene," *Reviews of Modern Physics* **83**, 407 (2011).

[62] S. Adam, E. H. Hwang, V. M. Galitski, and S. Das Sarma, "A self-consistent theory for graphene transport," *Proceedings of the National Academy of Sciences of the United States of America* **104***,* 18392 (2007).

[63] E. H. Hwang and S. Das Sarma, "Acoustic phonon scattering limited carrier mobility in two-dimensional extrinsic graphene," *Physical Review B* **77**, 115449 (2008).

[64] S. Pisana, M. Lazzeri, C. Casiraghi et al., "Breakdown of the adiabatic Born-Oppenheimer approximation in graphene," *Nature Materials* **6**, 198 (2007).

[65] D. K. Efetov and P. Kim, "Controlling electron-phonon interactions in graphene at ultrahigh carrier densities," *Physical Review Letters* **105**, 256805 (2010).

[66] T. Stauber, N. M. R. Peres, and F. Guinea, "Electronic transport in graphene: a semiclassical approach including midgap statesr densities," *Physical Review B* **76**, 205423 (2007).

[67] L. A. Ponomarenko, R. Yang, T. M. Mohiuddin et al., "Effect of a high-κ environment on charge carrier mobility in graphene," *Physical Review Letters* **102**, 206603 (2009).

[68] W. Zhu, V. Perebeinos, M. Freitag, and P. Avouris, "Carrier scattering, mobilities, and electrostatic potential in monolayer, bilayer, and trilayer graphene," *Physical Review B* **80**, 235402 (2009).

[69] S. Fratini and F. Guinea, "Substrate-limited electron dynamics in graphene," *Physical Review B* **77**, 195415 (2008).

[70] S. Rotkin, V. Perebeinos, A. G. Petrov, and Ph. Avouris, "An essential mechanism of heat dissipation in carbon nanotube electronics," *Nano letters* **9**, 1850 (2009).

[71] T. Ohta, A. Bostwick, J. L. McChesney, T. Seyller, K. Horn, and E. Rotenberg, "Interlayer interaction and electronic screening in multilayer graphene investigated

with angle-resolved photoemission spectroscopy," *Physical Review Letters* **98**, 206802 (2007).

[72] F. Guinea, "Charge distribution and screening in layered graphene systems," *Physical Review B* **75**, 235433 (2007).

[73] D. Ferry, *Transport in Nanostructure* (Cambridge University Press, Cambridge, United Kingdom, 2009), Chapter 2.

[74] E. H. Hwang and S. Das Sarma, "Screening-induced temperature-dependent transport in two-dimensional graphene," *Physical Review B* **79**, 165404 (2009).

[75] L. Pietronero, S. Strässler, H. R. Zeller, and M. J. Rice, "Electrical conductivity of a graphite layer," *Physical Review B* **22**, 904 (1980).

[76] X. Du, I. Skachko, A. Barker, and E. Y. Andrei, "Approaching ballistic transport in suspended graphene," *Nature Nanotechnology* **3**, 491 (2008).

[77] C. R. Dean, A. F. Young, I. Meric et al., "Boron nitride substrates for high-quality graphene electronics," *Nature Nanotechnology* **5**, 722 (2010).

[78] *https://www.qdusa.com/sitedocs/productBrochures/1070-002.pdf*

[79] V. P. Gusynin and S. G. Sharapov, "Unconventional integer quantum Hall effect in graphene," *Physical Review Letters* **95**, 146801 (2005).

[80] M. N. Carcassi and F Fineschi, "Deflagrations of H_2–air and CH_4–air lean mixtures in a vented multi-compartment environment," *Energy* **30**, 1439 (2005).

[81] O. T. Wehling, S. Yuan, A. I. Lichtenstein, A. K. Gein, and M. I. Katsnelson, "Resonant Scattering by Realistic Impurities in Graphene," *Physical Review Letters* **105**, 056802 (2010).

[82] S. Sarkar, H. Zhang, J. W. Huang, F. Wang, E. Bekyarova, C. N. Lau, and R. C. Haddon, "Organometallic hexahapto functionalization of single layer graphene as a route to high mobility graphene devices," *Advanced Materials* **25**, 1131 (2013).

[83] G. Giovannetti, P. A. Khomyakov, G. Brocks, V. M. Karpan, J. van de Brink, and P. J. Kelly, "Doping graphene with metal contact," *Physical Review Letters* **101**, 026803 (2008).

[84] W. E. Vargas, I. Rojas, D. E. Azofeifa, and N. Clark, "Optical and electrical properties of hydrided palladium thin films studied by an inversion approach from transmittance measurements," *Thin Solid Films* **496**, 189 (2006).

[85] N. N. Greenwood and A. Earnshaw, *Chemistry of the Elements*, 2nd Edition (Elsevier Butterworth-Heinemann, Oxford, United Kingdom, 1997), pp 1150-1151.

[86] Y. G. Sun, H. H. Wang, and M. G. Xia, "Single-walled carbon nanotubes modified with Pd nanoparticles: unique building blocks for high-performance, flexible hydrogen sensors," *Journal of Physical Chemistry C* **112**, 1205 (2008).

[87] D. Jena and A. Konar, "Enhancement of carrier mobility in semiconductor nanostructures by dielectric engineering." *Physical Review Letters* **98**, 136805 (2007).

[88] A. Konar, T. Fang, and D. Jena, "Effect of high-κ gate dielectrics on charge transport in graphene-based field effect transistors," *Physical Review B* **82**, 115452 (2010).

[89] M. J. Hollander, M. LaBella, Z. R. Hughes et al., "Enhanced transport and transistor performance with oxide seeded high-κ gate dielectrics on wafer-scale epitaxial graphene," *Nano letters* **11**, 3601 (2011).

[90] M. S. Bresnehan, M. J. Hollander, M. Wetherington, M. LaBella, K. A. Trumbull, R. Cavalero, D. W. Synder, and J. A. Robinson, "Integration of hexagonal boron nitride

80

with quasi-freestanding epitaxial graphene: toward wafer-scale, high-performance devices," *ACS Nano* **6**, 5234 (2012).

[91] M. J. Hollander, A. Agrawal, M. S. Bresnehan, M. LaBella, K. A. Trumbull, R. Cavalero, D. W. Synder, S. Datta, and J. A. Robinson, "Heterogeneous integration of hexagonal boron nitride on bilayer quasi‐free‐standing epitaxial graphene and its impact on electrical transport properties," *physica status solidi (a)* **210**, 1062 (2013)